CORA Cork Open Research Archive
Cartlann Taighde Oscailte Chorcaí

Title	3D modelling the long-term ageing performance of a CERN tunnel
Authors	Xiao, Zhipeng;Wang, Chao;Peng, Chuanyang;Osborne, John Andrew;Li, Zili
Publication date	2026-03-06
Original Citation	Xiao, Z, Wang, C, Peng, C, Osborne, J A & Li, Z 2026, '3D modelling the long-term ageing performance of a CERN tunnel', KSCE Journal of Civil Engineering, vol. 30, no. 7, 100570, pp. 1-22. https://doi.org/10.1016/j.kscej.2026.100570
Type of publication	Article (peer-reviewed)
Link to publisher's version	https://www.scopus.com/pages/publications/105039437256 - 10.1016/j.kscej.2026.100570
Rights	© 2026, authors. Published by Elsevier Inc. on behalf of Korean Society of Civil Engineers. This is an open access article under the CC BY license (http://creativecommons.org/licenses/by/4.0/) - https://creativecommons.org/licenses/by/4.0/
Download date	2026-11-15 14:00:43
Item downloaded from	https://hdl.handle.net/10468/19488

UCC
University College Cork, Ireland
Coláiste na hOllscoile Corcaigh

KSCE Journal of Civil Engineering 30 (2026) 100570

Contents lists available at ScienceDirect

KSCE Journal of Civil Engineering

journal homepage: www.elsevier.com/locate/kscej

3D modelling the long-term ageing performance of a CERN tunnel

Zhipeng Xiao [a], Chao Wang [b,*], Chuanyang Peng [b], John Andrew Osborne [c], Zili Li [b,d]

[a] Department of Geotechnical Engineering, Guangdong Hualu Transportation Technology Company Limited, Guangzhou, China
[b] School of Engineering and Architecture, University College Cork, Cork, Ireland
[c] European Organisation for Nuclear Research, CERN, 1211 Geneva 23, Switzerland
[d] Irish Centre for Research in Applied Geosciences, University College Dublin, Ireland

ARTICLE INFO

Keywords:
Tunnel hydromechanical deterioration
Marl swelling
Ground layering
Ground permeability anisotropy
Long-term ageing performance
CERN tunnel
Numerical modelling
Geodetic and DFOS field monitoring

ABSTRACT

Many operational tunnels worldwide experience progressive deformation due to hydraulic drainage failure, structural deterioration, ground rheological behaviour, and other factors. This study presents a three-dimensional finite element analysis of an ageing horseshoe-shaped tunnel at CERN (European Organization for Nuclear Research), excavated in molasse rock, to investigate the effects of tunnel lining hydraulic and mechanical deterioration, marl swelling, ground layering, and ground permeability anisotropy. Hydraulic deterioration, caused by drainage clogging, is modelled by reducing lining permeability, while mechanical deterioration is represented by decreasing the lining stiffness. Model validation is conducted by comparing simulated results with geodetic and distributed fibre optic sensing (DFOS) data at a representative tunnel section. Parametric studies are then performed to assess the effects of ground layering and permeability anisotropy. Results show that: (1) hydraulic deterioration leads to vertical elongation, mechanical deterioration to tunnel contraction, and their combination to more severe deformation; (2) marl swelling is the dominant mechanism, with deterioration effects being secondary; (3) inclined tunnel alignment through stratified ground induces varying deformation modes due to geological heterogeneity; and (4) permeability anisotropy accelerates groundwater pressure buildup, amplifying vertical elongation. These findings highlight the complex interplay of deterioration and geological factors in ageing tunnels and demonstrate the need for 3D hydromechanical modelling to support long-term performance assessment and maintenance.

1. Introduction

Aging tunnels worldwide commonly exhibit defects such as cracks and water leakage, which develop over time and pose increasing risks to tunnel serviceability and/or safety while escalating maintenance costs. Regardless of geological conditions or tunnel lining types, continuous tunnel deterioration is primarily attributed to factors such as surrounding ground rheological behaviour, lining structural degradation and hydraulic deterioration throughout the tunnel's lifespan (Sandrone & Labiouse, 2010).

Tunnel hydraulic deterioration is typically categorised into two main types: (1) water leakage and increased lining permeability in originally watertight tunnels, and (2) blocked drainage and decreased lining permeability in tunnels initially designed as drains. Segmental tunnels are generally designed to be watertight with an allowable level of leakage, meaning hydraulic deterioration in such tunnels often leads to local leakage and increased permeability, exemplified by leakage through cracks and joints (Shin et al., 2012). Numerous studies have analysed the impact of local leakage at segmental tunnel joints on tunnel deformation and surrounding pore water pressure through analytical and numerical methods (Reddi et al., 2000; Shin et al., 2012; Wu et al., 2014, 2020; Yoo, 2017; Zhang et al., 2017, 2015). Conversely, for tunnels functioning as drains, such as rock mountain tunnels, waterproofing and drainage systems are essential for discharging groundwater to mitigate the accumulation of pore water pressure on the lining (Li et al., 2018). Drainpipes and filter layers are commonly used to collect groundwater and facilitate seepage. Over time, however, the drainage capacity of the initially drained tunnel may decline due to filter/-drainpipe clogging, which can be attributed to the accumulation of transported materials, and increased loads from surrounding rock or concrete placement (Shin et al., 2005; Yoo, 2016). This reduction in drainage efficiency leads to elevated pore water pressure, lining deterioration, and structural damage (Jung et al., 2013; Reddi et al., 2000; Shin et al., 2010). Therefore, understanding the influence of such tunnel

* Corresponding author.
E-mail address: chao.wang@ucc.ie (C. Wang).

https://doi.org/10.1016/j.kscej.2026.100570
Received 20 August 2025; Received in revised form 7 January 2026; Accepted 2 March 2026
Available online 6 March 2026
1226-7988/© 2026 The Authors. Published by Elsevier Inc. on behalf of Korean Society of Civil Engineers. This is an open access article under the CC BY license (http://creativecommons.org/licenses/by/4.0/).

hydraulic deteriorations is crucial for maintaining aging tunnels.

Although the degradation of tunnel geotextile filter drainage capacity has been extensively studied (Jang et al., 2015; Kim et al., 2020; Murillo et al., 2014), research on how it impacts tunnel ageing performance remains limited. Shin et al. (2005) pioneered the investigations into the effects of tunnel drainage system deterioration on New Austrian Tunnelling Method (NATM) tunnels. Subsequent studies examined the impact of hydraulic deterioration due to clogging on tunnel lining behaviour (Shin et al., 2014; Shin, 2008, 2010). Findings indicate that hydraulic deterioration impedes water flow into the tunnel, causing asymmetric development of pore water pressure and associated damage on the secondary tunnel lining. Yoo (2016) further analysed the structural impact of geotextile filter deterioration using FE simulations. Additionally, Li et al. (2015) explored the long-term behaviour of a cast-iron cross passage tunnel in stiff London clay, focusing on ground settlement and structural behaviour under varying lining permeability. However, most studies have only considered idealised fully permeable or impermeable linings, neglecting the progressive changes in lining permeability over time. Furthermore, past research has predominantly focused on circular tunnels, overlooking non-circular cross-sections such as horseshoe-shaped tunnels, which are widely used in road and mountain tunnels.

Beyond hydraulic deterioration, tunnel linings also experience mechanical, physical, chemical, and/or biological degradation over time (Idris et al., 2009). Structural defects such as cracks, convergence, and local spalling indicate declining concrete mechanical properties. Usman and Galler (2013) studied the long-term degradation of sprayed concrete linings using three-dimensional FE analysis, simulating the gradual reduction in stiffness to assess stress distribution and tunnel stability. Similarly, Sandrone and Labiouse (2010) modelled the effect of tunnel lining structural deterioration on its performance by simulating the reduction of the mechanical properties of both the rock mass and the lining. More recently, Showkati et al. (2021) developed a methodology to predict long-term tunnel behaviour considering both rock weathering and concrete deterioration.

In addition to tunnel deteriorations, the rheological behaviour of the surrounding ground significantly influences tunnel performance over time. Previous studies have found that the long-term viscoelastic and plastic deformations of the ground can lead to progressive tunnel convergence, increased stress redistribution, and time-dependent ground-lining interaction effects. Nie and Zhang (1994) found that the time-dependent deformation of tunnel shotcrete lining is strongly associated with the creep of surrounding rock layer, which shares the similar conclusion with Kovári and Staus (1996). Zhang et al. (2021) summarised that rock creep leads to excessive deformation of Erlangshan tunnel in China only 3 years after operation based on numerical results from discrete element modelling. Do et al. (2020) assessed the time-dependent reliability of a deep circular tunnel with the rheological characteristic of the surrounding rock mass and the sequential construction of liners considered and found that the creep behaviour of the rock mass contributed to the increase of compressive radial and tangential stresses in both the primary and secondary liners. These studies showed the neglection of the creep effect may lead to significant underestimation of the tunnel responses and understanding these long-term rheological effects is crucial for assessing tunnel stability.

With advancements in numerical modelling, soil-fluid coupled FE simulations have become increasingly utilised to predict long-term ground movements and tunnel behaviour (Li et al., 2016; Showkati et al., 2021; Tornborg et al., 2021; Wang et al., 2012; Wongsaroj et al., 2013; Wu et al., 2020).

However, many existing studies still adopt simplified assumptions like laterally/longitudinally uniform ground conditions and idealised hydraulic boundary conditions, and rarely consider inclined tunnels that traverse multiple strata with contrasting stiffness-permeability properties. As a result, the combined influence of stratigraphic variability, time-evolving drainage deterioration, lining mechanical deterioration, and swelling of weak marl on the long-term deformation patterns of non-circular tunnels remains insufficiently understood and is seldom evaluated against long-term in-situ monitoring.

In light of the limitations and gaps in previous research, this study presents a three-dimensional FE investigation of the long-term ageing performance of a horseshoe-shaped, concrete-lined tunnel in the molasse rock mass at CERN. The analysis integrates marl swelling with progressive hydraulic deterioration and lining stiffness degradation to evaluate the deformation evolution of an inclined tunnel. The numerical predictions are compared against both geodetic and DFOS monitoring measurements. In addition, a parametric study is conducted to examine how variations in ground-layer configuration and permeability anisotropy affect tunnel response across representative tunnel sections at CERN.

2. Background of CERN TT10 tunnel

CERN, short for European Organisation for Nuclear Research, is located near Geneva on the Swiss-French border and is a renowned particle physics laboratory operating the world's most powerful circular particle accelerator within an extensive underground tunnel network spanning over 70 km (Fig. 1(*a*)). This underground tunnel network, comprising deep underground rings, caverns, shafts, and tunnels, was excavated in weak to medium-strong sedimentary rock known as molasse.

A particular engineering concern is the TT10 tunnel, an inclined transfer tunnel connecting the beam accelerator of the PS (Proton Synchrotron) tunnel to the SPS (Super Proton Synchrotron) tunnel (Fig. 1(*b*)). Unlike the main ring tunnels, which feature a circular cross-section, TT10 was constructed in the 1970s with a horseshoe-shaped cross-section of 5.1 m in outer diameter, as illustrated in Fig. 1(*c*). The tunnel is supported by a double lining system: a primary lining of sprayed concrete and a secondary lining of cast-in-situ concrete. In addition, a drainage system was incorporated, comprising two small drainage pipes along both sides of the tunnel invert, a main drainage pipe beneath the tunnel floor, and a waterproofing membrane positioned between the shotcrete and concrete lining.

Over more than four decades of operation, the tunnel has experienced progressive deterioration due to complex ground conditions and tunnel deteriorations. Field observations and measurements indicate the development of significant structural issues, including visible cracks, water infiltration, and deformation (as demonstrated in Fig. 2). Notably, the tunnel floor beneath the accelerator beamline has exhibited progressive heaving and cracking (Fig. 2(*c*)), necessitating regular realignment of beamline to maintain serviceability. To monitor long-term tunnel movements, CERN initiated convergence surveys using an automatic total station in 2013.

Recent investigations have revealed extensive tensile and compressive cracks in the tunnel lining (Di Murro et al., 2016), underscoring the need for a deeper understanding of the mechanisms driving its continuous structural deterioration. Of particular concern is the damage to drainage pipes and the accumulation of calcite deposits, which suggest clogging of the drainage system and a consequent alteration of the tunnel's hydraulic boundary conditions. Early signs of groundwater ingress accompanied by calcite deposits were observed in 2008, followed by camera inspections that confirmed drainage pipe damage and calcite deposition (see Fig. 2(*d*)).

3. Three-dimensional finite element modelling

A series of three-dimensional finite element numerical analyses were performed to gain insight into the long-term behaviour of the ageing TT10 tunnel under various factors. The hydraulic deterioration of the tunnel was simulated by progressively reducing its drainage capacity, while structural degradation was represented by decreasing the stiffness of the tunnel lining. Additionally, the influence of the swelling marl

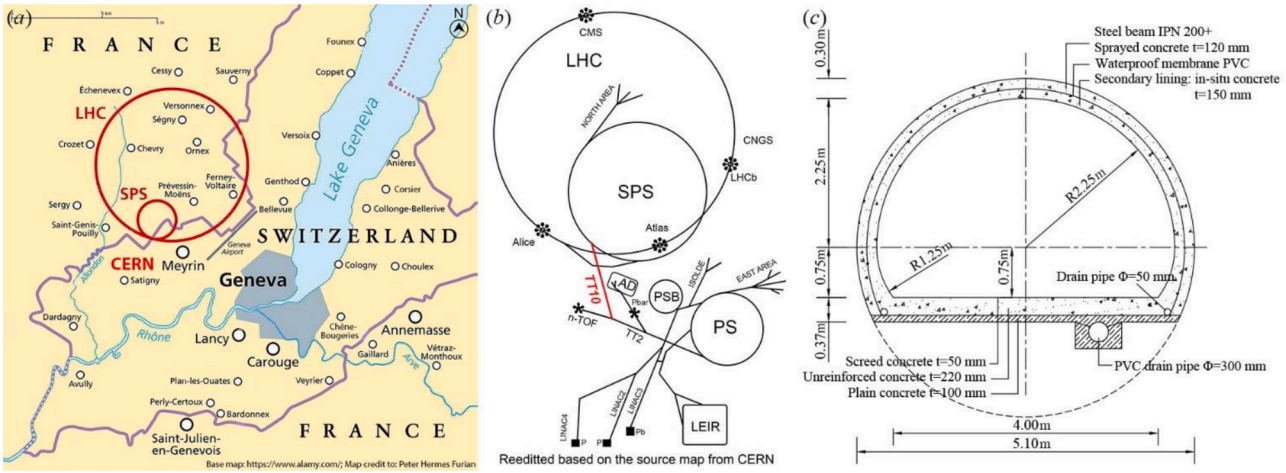


Fig. 1. TT10 tunnel location and cross-section (adapted from Wang et al. (2024)).



(*a*) circumferential cracks along cross section

(*b*) longitudinal cracks at tunnel axis level

(*c*) longitudinal cracks at tunnel floor

(*d*) water ingress with calcite deposits

Fig. 2. Field observations of deteriorations in TT10 tunnel.

ground layer on tunnel performance was examined to assess its contribution to the observed structural deformation.

3.1. Numerical model and boundary conditions

This study takes the inclined TT10 tunnel as a case study. The tunnel has been observed with signs of deterioration, including lining movement and floor heaving in recent years. The tunnel traverses multiple rock layers with an incline of approximately 6 %, with depths ranging from 23.9 m to 31.1 m below the ground surface in the numerical model. The ground profile adopted for the FE analysis is based on in-situ ground investigations, borehole logs, and excavation face-logs (CERN, 1972; Di Murro, 2019; GADZ, 2016a, b), as illustrated in Fig. 3. The adopted profile comprises a 19 m thick layer of moraine deposits overlying a 38 m thick red molasse region with interbedded layers resting on sandy marl.

To optimise computational efficiency, a half model of the TT10 tunnel was developed using ABAQUS (2019), leveraging symmetry considerations, as shown in Fig. 4. The model dimensions extend 120 m in length, 180 m in width, and 70 m in height to minimise boundary

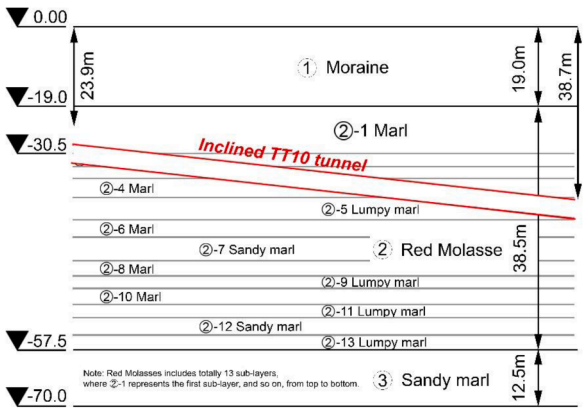


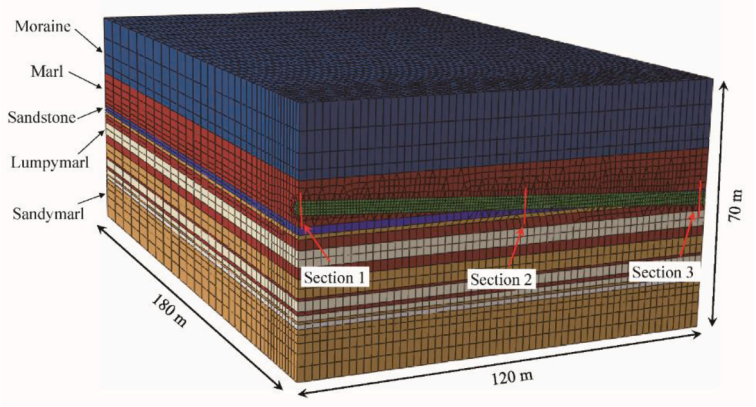
Fig. 3. Ground profile around a section of the TT10 tunnel.

effect. Lateral displacement boundaries were constrained in the horizontal direction while allowing vertical movement, with the front face set as a symmetry plane. The bottom boundary was fixed, while the top boundary remained free.

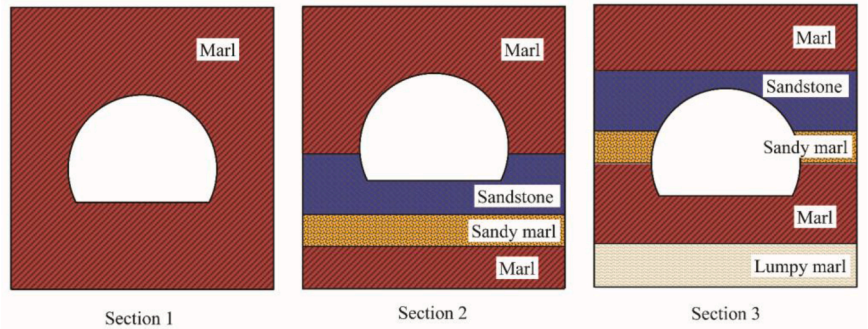
The related physical and mechanical properties for the ground units (Table 1) were adopted from prior site investigations and ground characterisation at TT10 (Di Murro, 2019; GADZ, 2016a, b), based on borehole and excavation face-logging and associated geotechnical reporting. The permeability anisotropy of layers of red molasse is also considered with the ratio of horizontal permeability to vertical permeability (k_h/k_v) to be 10 first, followed by a relevant parametric analysis. The initial pore water pressure was assumed to be hydrostatic with the water table at 4.0 m below the ground surface. During both short-term excavation and long-term operation phases, the ground stress remained within the rock yield surface, with the stress path staying well below the failure line. Consequently, a linear-elastic perfectly plastic Mohr-Coulomb constitutive model was implemented to simulate the behaviour of rock layers surrounding the tunnel. For the tunnel structure, the actual tunnel lining comprising of primary and secondary lining was modelled as a single equivalent linear elastic layer in the FE model as the primary and secondary linings are strongly bonded and respond in unison to external loads, sharing similar approaches reported in previous studies (Wang et al., 2025). Therefore, the equivalent tunnel lining was assigned with an elastic modulus E of 20 GPa and a Poisson's ratio υ of 0.25. Since the primary focus of this study is the long-term ageing performance of the TT10 tunnel, the excavation process was simplified in the model. Additionally, the tunnel lining was represented as shell elements, as further detailed in Section 3.2.

Table 1
Summary of physical and mechanical properties for all ground units.

Variable	Lumpy marl	Marl	Sandy marl	Sandstones	Moraine
Saturated density γ_{sat} [kN/m^3]	20	24	24	24	22.5
Earth pressure coefficient at rest k_0	1.5	2.0	2.0	2.0	2.0
Young's modulus E [MPa]	220	350	1250	2200	50
Poisson's ratio υ	0.2	0.2	0.2	0.2	0.3
Effective cohesion c' [MPa]	0	3	11	15	0.1
Friction angle φ' [°]	25	-	-	-	31
Dilatancy ψ [°]	0	2	2	2	2
Permeability k_v [m/s]	1×10^{-10}	1×10^{-9}	1×10^{-9}	1×10^{-8}	1×10^{-7}



(*a*) Mesh of the FE model



(*b*) ground layering at the selected tunnel sections

Fig. 4. Finite element model of TT10 tunnel and three representative sections.

3.2. Tunnel numerical modelling sequence

This study focuses on the long-term ageing performance of the TT10 tunnel, rather than its short-term construction process. Consequently, a simplified construction sequence was assumed in the FE modelling. The stress release method was employed instead of simulating the full excavation history, given its negligible impact on incremental deformation. At the initial tunnel excavation stage, the nodal loads around the tunnel boundary were reduced by a certain percentage (e.g., 50 %) following the removal of ground elements inside the tunnel, simulating stress relief prior to lining installation. The 50 % stress release ratio was selected following previous studies, as no measured data is available (Li et al., 2015; Wang et al., 2024). Since the primary concern is incremental displacement after tunnel deterioration and marl swelling, both the stress release ratio and the actual construction history are expected to have minimal influence on the results. Following excavation, shell elements were attached to the tunnel boundary to represent the lining. The construction process was assumed to occur under undrained conditions, considering the relatively short duration of the excavation process. In the post-construction stage, tunnel drainage was introduced. Since TT10 is equipped with a drainage system, a fully drained condition was assumed during the long-term operation stage, representing approximately 40 years of service with minimal deterioration from 1972. This stage accounts for the gradual dissipation of pore water pressure around the tunnel over time. After this long-term operation stage, the impact of tunnel hydraulic and mechanical deterioration, together with the influence of the swelling marl, was modelled on both an individual and coupled basis. The tunnel lining permeability is reduced in the hydraulic deterioration stage to simulate the decreasing liner drainage capacity due to hydraulic deterioration, while the liner stiffness is decreased to model the structural degradation with time in structural deterioration stage. The swelling behaviour of the marl layer was modelled after the long-term operation stage. The full sequence of tunnel modelling steps assumed in the FE analysis is summarised in Table 2.

3.3. Modelling the impact of hydraulic deterioration

The hydromechanical interaction between tunnel and surrounding ground was modelled by assigning a drainage-only flow surface to the tunnel boundary around its entire circumference in ABAQUS. This boundary condition governs drainage behaviour by assuming that pore fluid flow is proportional to the pore pressure at the tunnel lining extrados. The drainage-only surface permits water flow from the ground into the tunnel while preventing backflow, thereby providing a more realistic representation of ground-lining drainage interactions.

Recent studies (e.g., Wongsaroj et al. (2013)) have emphasised the significance of the relative permeability between the tunnel lining and the adjacent ground in determining both flow rates and pore water pressures acting on the lining. Instead of considering absolute permeability values, the relative permeability ratio RP is defined as: $RP = k_l/k_s$ where k_l is the permeability coefficient of the lining and k_s is the permeability coefficient of the ground. In general, the tunnel is considered fully permeable relative to the surrounding ground if $RP > 10$, whereas the tunnel is nearly impermeable if $RP < 0.001$ (Li et al., 2015). In this study, the relative lining-ground permeability RP is defined as the lining permeability relative to the permeability of the marl, the primary geological formation embedding the tunnel. This parameter will be used in later sections to assess the impact of declining tunnel drainage capacity on lining performance in the long term.

As mentioned earlier, the deterioration of tunnel hydraulic conditions is primarily attributed to clogging of drainage pipes and filters. The reduction in tunnel drainage capacity can be numerically simulated by decreasing the lining permeability (Shin et al., 2012; Wang et al., 2024). That is, by decreasing the magnitude of k_T, which is the seepage coefficient of the drainage-only flow surface in ABAQUS, the tunnel becomes less permeable in comparison to the surrounding ground (i.e., smaller RP). Previously, the lining permeability was varied to cover a range of relative permeability ratios from 10^{-3} to 10^{3}; In particular, two extreme hydraulic boundary conditions were considered: (1) impermeable lining ($RP = 0.001$) and (2) fully permeable lining ($RP = 1000$), following previous studies on relative permeability RP, as shown in Fig. 5. The former scenario represents a fully clogged drainage system (fully impermeable), leading to complete hydraulic deterioration, whereas the latter represents an idealised fully drained tunnel (fully permeable) (Laver et al., 2017; Wang et al., 2025; Wongsaroj et al., 2013).

The clogging of tunnel drainage system can be attributed to a number of factors, such as crystallisation, particle deposition, filter squeezing and hydraulic gradient. The progressive reduction in lining drainage capacity is a direct consequence of these factors and is generally assumed to develop at a constant rate over time (Li et al., 2020). Thus, by assuming a constant rate for drainage blocking, the change of the logarithm of lining permeability is considered to be directly proportional to the deterioration rate as $\log k - \log k_0 = R_s \times t$ where k_0 represents the original permeability and R_s is the deterioration rate. Similarly, Zhang et al. (2022) assumed the relationship between the permeability coefficient of the lining and the analysis step as $k_n = k_0(3/4)^n$ where $n = t/90$, t and n are the time and analysis steps, respectively. The TT10 tunnel in this paper is designed as drains throughout its service lifetime, with an initial permeability for the equivalent lining of 6.67×10^{-08} m/s. In the absence of extensive field measurements and the inability to conduct in-situ tests, this study follows simplifying research assumption, modelling the tunnel lining permeability as evolving linearly from a fully permeable to an impermeable state starting from 2013 when field inspections of the CERN TT10 tunnel revealed calcite deposition, worsening pipe damage, etc. As it is hard to determine the current hydraulic status, the tunnel is assumed to gradually deteriorate hydraulically with time, with it becoming fully impermeable as an upper bound (UB, $RP = 0.0001$) and becoming partially impermeable as a lower bound (LB, $RP = 0.1$), as shown in Fig. 5. The chosen upper and lower bounds ($RP = 0.0001$ and $RP = 0.1$) therefore serve to bracket the possible hydraulic scenarios of the current state. The adoption of a linear hydraulic deterioration may mainly influence the predicted timing/rate of tunnel deformation development, whilst the assumption of a simplified uniform lining permeability may neglect localised effects (e.g., asymmetric distortion) that could arise from spatially varied clogging in practice. Nevertheless, due to lack of non-linear or non-uniform lining deterioration data, this study therefore only adopts the aforementioned linear and uniform lining assumptions. These assumptions still can represent the general drainage decline, and therefore capture the clogging-induced deformation mechanism.

Table 2
Modelling stages assumed in the FE analysis.

Stages	Stage Description
Geostatic equilibrium	1. Initial geostatic equilibrium state
Excavation modelling	2.1. Excavation of soil elements and tunnel nodal force reduction to 50 % (undrained)
	2.2. Activate the lining elements and tunnel nodal force reduction to 0 % (undrained)
Long-term operation	3. Long-term ground consolidation that permits water flows for around 40 years
Tunnel deterioration or Marl swelling	4.1. Hydraulic deterioration: reduce the lining permeability
	4.2. Mechanical deterioration: reduce the lining stiffness
	4.3. Marl swelling: model the viscoelastic creep behaviour of marl

3.4. Modelling the impact of mechanical deterioration

Like other concrete structures, concrete tunnel lining inevitably de-

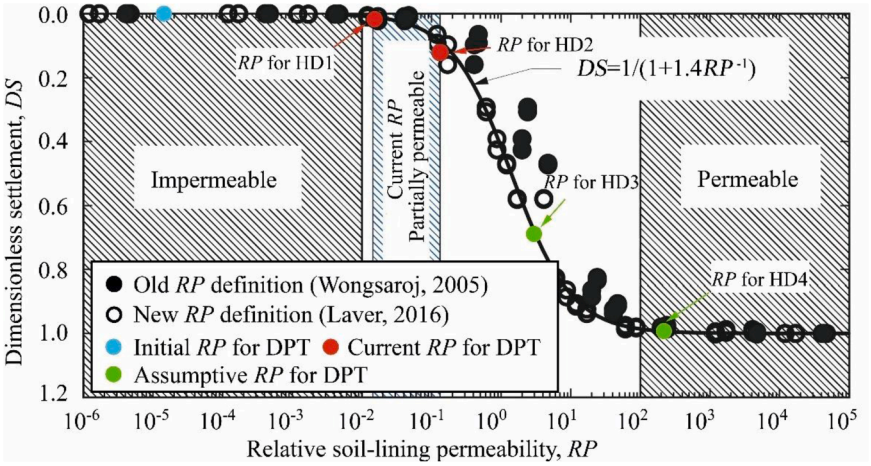


Fig. 5. Previous relative soil-lining permeability ratios (Laver et al., 2017; Wang et al., 2025; Wongsaroj, 2005).

teriorates in the long term: it usually begins on exposed surfaces under water pressure, and may exacerbate through cracks and joints (Sandrone & Labiouse, 2010). When the waterproofing system fails, the final lining becomes vulnerable to external degradation at both the intrados and extrados, leading to a reduction in tunnel lining mechanical properties. According to Sandrone and Labiouse (2010), the evolution of the Young's modulus E and the compressive strength f_c of the concrete lining can be described as follows: $\delta E/E0 = (E_0 - E)/E_0 = k_m \times \delta d$ and $\delta f_c / f_{c0} = (f_{c0} - f_c)/f_{c0} = k_r \times \delta d$, where E_0 and f_{c0} represent the original Young's modulus and the compressive strength, while k_m and k_r are the material related coefficients, and are respectively, 0.66 and 0.76 for a medium-quality concrete; δ_d represents the ratio of the deteriorated depth to the initial thickness, i.e., $\delta_d = X_d/d_s$, in which X_d and d_s represent the deteriorated thickness and the initial thickness of lining respectively. Usually, the deteriorated thickness, X_d, is considered proportional to the square root of time, t, as $X_d = a \times \sqrt{t}$. The degradation rate a is a material constant, which depends on the external environment and concrete quality. The degradation of the lining thickness due to Calcium leaching, for example, in an underground environment, can reach a maximum value of 100 to 120 mm in 100 years (Showkati et al., 2021; Yokozeki et al., 2004), which gives the estimated degradation rate $a = 5.0 \sim 6.0 \times 10^{-4}$ ($m/\sqrt{days}$). Showkati et al. (2021) adopted the same assumption to predict the long-term stability of tunnels subject to the impact of mechanical deterioration. In Usman and Galler (2013), the gradual mechanical deterioration of tunnel liners under various attacks was simulated by reducing the Young's modulus, cohesion and friction angle of the sprayed concrete lining.

In practice, determining the exact rate of lining mechanical deterioration in ageing tunnels like TT10 is highly challenging due to complex interactions between material properties and environmental factors. Therefore, this FE study aims to qualitatively assess the effect of lining mechanical deterioration on the long-term structural behaviour of the TT10 tunnel following similar stiffness assumption from Sandrone and Labiouse (2010). This study focuses solely on stiffness reduction because the tunnel remains in service and no signs of structural failure have been reported. As such, the deformation behaviour is governed primarily by stiffness loss rather than failure processes, and modelling strength reduction was deemed unnecessary for capturing the dominant ageing mechanisms under service conditions. In the case of TT10, the reduction of tunnel lining stiffness is considered to be caused by the coupled effect of concrete cracking, spalling and water ingress, which could contribute to a higher rate of deterioration. Therefore, a higher rate of 1.0×10^{-03} $m/\sqrt{day}$ (reflecting an accelerated degradation with sustained cracking, spalling and water ingress) is assumed as the UB for modelling TT10 mechanical deterioration from 2013, and a smaller rate of 5.0×10^{-04} $m/\sqrt{day}$ is assumed as the LB (representing a more moderate deterioration rate typical of less aggressive but cumulating ageing effects observed in older tunnels). In the FE analysis, this can be achieved using the defined field variables in ABAQUS, where the material properties are linked to field variables and varied as functions of time in the designated calculation step.

3.5. Modelling the impact of marl swelling

The time-dependent behaviour of rocks acts as a crucial role in the long-term deformation of the tunnel. As reported in Fern et al. (2018), the swelling of the marl layer was encountered during the tunnel excavation in CERN TT10 tunnel, and the rock sample tests also demonstrated such a phenomenon. The swelling behaviour of the marl layer should be considered to account for the ongoing TT10 tunnel deformation. Previous studies have shown that such behaviour can be modelled by viscoelastic models (creep models), such as viscoelastic-plastic models (CVISC), elastic-visco-plastic models (VIPLA), Nishihara model, modified Nishihara model, etc. (Liu et al., 2021; Bonini et al., 2009; Yang et al., 2014). Therefore, to investigate this impact, the selection of creep models is key to a successful simulation of the realistic rock performance. Previous studies have proposed many common creep constitutive models including Maxwell model and Kelvin model, and also many specific creep constitutive models for various specific and general rock types under different loading and environmental conditions, such as classical Nishihara model (Wang et al., 2023) and UCC creep model (Wang et al., 2019). For the marl in this study, it is believed to have not entered the tertiary creep stage, indicating that it still can be regarded as a viscoelastic material. To simulate such viscoelastic material, Burgers model in Fig. 6 is believed to be one of the creep models that can better represent the realistic deformational characteristic of rock attenuation creep (primary creep) and constant velocity creep (secondary creep). It is composed of a Maxwell model and a Kelvin model, where the Kelvin model is used to describe the primary creep stage while the Maxwell model is mainly

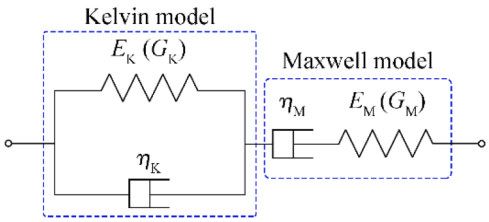


Fig. 6. Burgers model comprising of Kelvin and Maxwell model.

adopted to describe the instantaneous strain and secondary creep stage (Wang & Li, 2018).

The formulations of the 1D and 3D Burgers model are listed below, respectively (Wang & Li, 2018):

$$\text{One dimensional model}: \ \varepsilon_B = \frac{\sigma}{E_M} + \frac{\sigma \cdot t}{\eta_M} + \frac{\sigma}{E_K} \cdot \left[1 - \exp\left(-\frac{E_K \cdot t}{\eta_K}\right)\right]$$

$$\text{Three} - \text{dimensional model}: \ \varepsilon_B^T = \frac{\sigma_1 - \sigma_3}{3} \cdot \left\{\frac{1}{3K_M} + \frac{1}{G_M} + \frac{t}{\eta_M} + \frac{1}{G_K} \cdot \left[1 - \exp\left(-\frac{G_K \cdot t}{\eta_K}\right)\right]\right.$$

where σ is axial stress; t is time; E_M and η_M are the elastic modulus and viscosity coefficient of the Maxwell model, respectively; E_K and η_K are the elastic modulus and viscosity coefficient of the Kelvin model, respectively; G_K is the shear modulus of the Kelvin model; and G_M and K_M are the shear modulus and bulk modulus of the Maxwell model, respectively; σ_1 and σ_3 denote the major, and minor principal stresses, respectively.

The acquisition of the Burgers model parameters typically is carried out by applying the curve fitting technique to the available rock creep experimental strain-time curves. Fig. 7 compares the computed strain-time results using Burgers model against the experimental data from creep tests on the marl rock in CERN tunnel. It is demonstrated that Burgers model can depict curves of the primary and secondary creep phases of the marl rock. Through the adoption of the Burgers model mentioned above and the application of curve fitting technique, the relevant Burgers model parameters are obtained as listed in Table 3.

Table 3
Burgers model creep parameters obtained by applying the curve-fitting on the test data.

σ_1 (kPa)	K (GPa)	G_M (GPa)	G_K (GPa)	η_M (GPa•day)	η_K (GPa•day)
1550	0.62	0.37	0.36	10.34	0.35
2400	0.83	0.72	0.57	60.19	2.11

The viscosity unit's standard conversion from GPa•day to Pa•s is 1GPa•day = 8.64 = × = 10^{13m} Pa•s

4. Tunnel ageing performance comparison

4.1. Field monitoring measurements

4.1.1. Geodetic monitoring data

Conventional geodetic monitoring using automatic total stations to capture liner deformation was conducted on a total of seven cross-sections along the TT10 tunnel, with each section comprising six reference targets deployed on the tunnel lining at various locations, as shown in Fig. 8. The geodetic monitoring of six cross-sections (from profile P1-P6) started in 2013 during a CERN shutdown, while cross-section profile P0 only began in 2015 as the two-year shutdown drew to a close.

As the inclined TT10 tunnel runs through different ground profiles and depths in the longitudinal direction, three tunnel cross-sections were chosen (Fig. 4), and one representative tunnel cross-section at the depth of 27.5 m is selected for specific investigation in this paper (Section 2). Section 1 is fully embedded in the marl layer in the upper stream of the tunnel (Figure 4(*a*)), while the representative cross-Section 2 locates in the middle of the inclined tunnel model, with tunnel crown and tunnel axis level embedded in the weak marl layer and the tunnel invert in the 2.1m-thick sandstone layer (Figure 4(*b*)). Section 3 is surrounded by multiple layers of ground. Section 2 is selected as the representative section for detailed investigation because it coincides with the location of monitoring rings shown in Figure 8(a) (Section 2 from the numerical model corresponds to the geodetic monitoring profile P0 in Figure 8(a)), allowing direct comparison and validation of numerical results against field measurements, where Section 1 and Section 3 lack corresponding DFOS instrumentation, limiting their suitability for in-depth numerical-experimental correlation. Field measurements recorded by the total station from year 2015 for P0 are shown in the following Fig. 9.

4.1.2. Distributed fibre optic sensing data

In addition to geodetic monitoring, a trial DFOS system based on Brillouin optical time-domain analysis was installed at two zones of the TT10 tunnel to monitor their long-term performance starting from 2014, as shown in Figure 10(*a*). The first zone consists of the deployment of 7

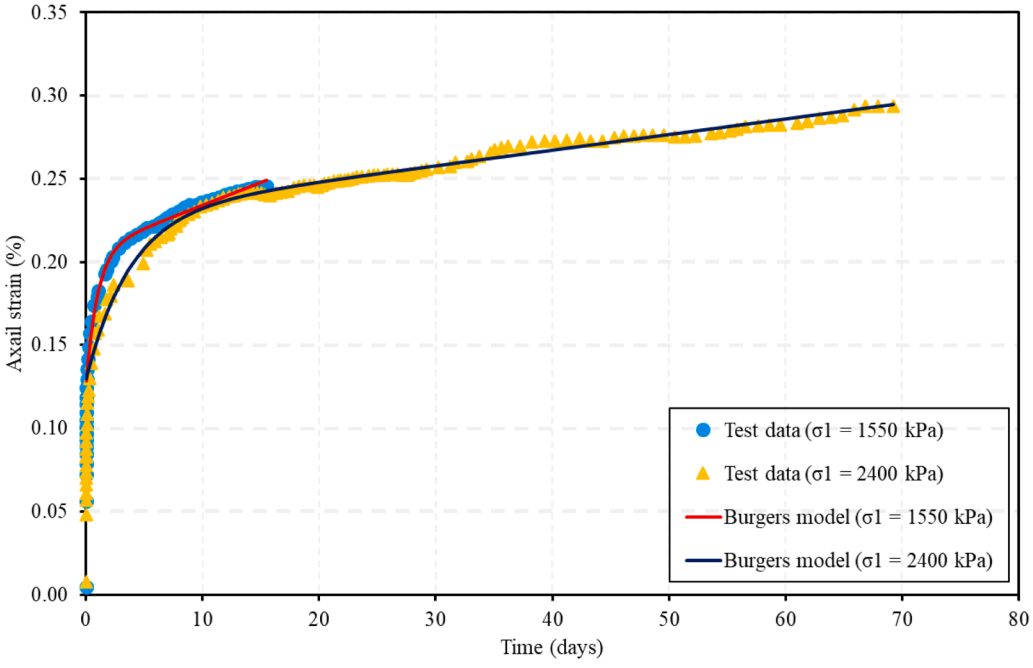


Fig. 7. The comparison between the Burgers model and the experiment curves.

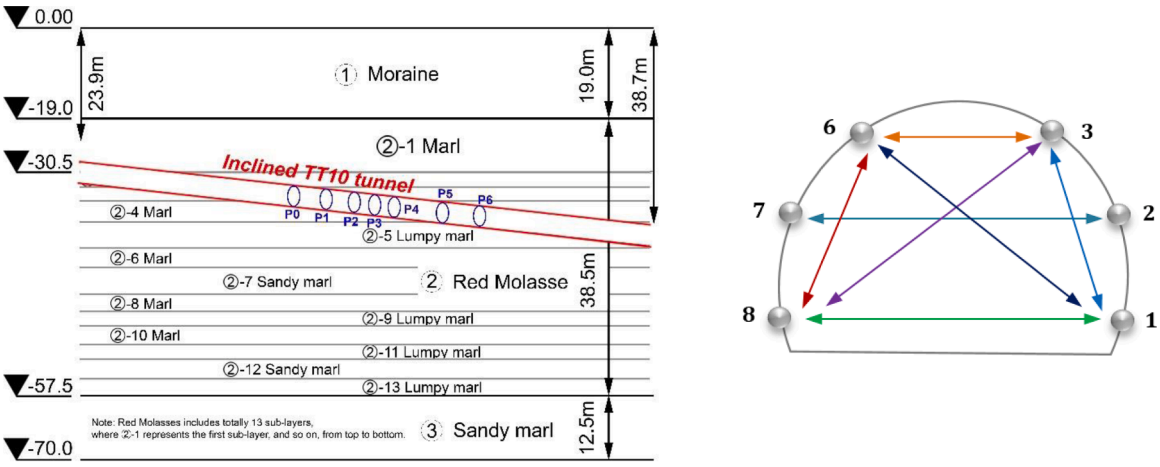


Fig. 8. Geodetic measuring location and deployment along TT10 tunnel.

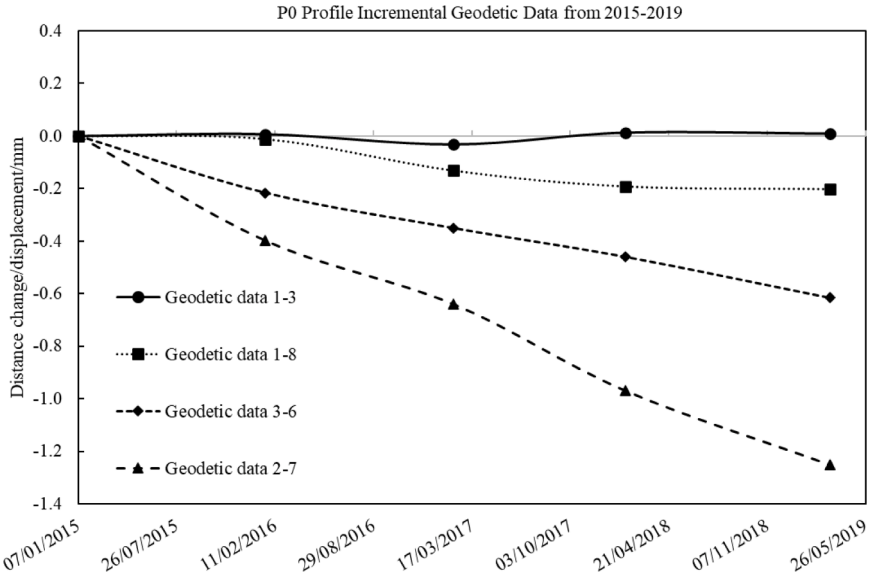
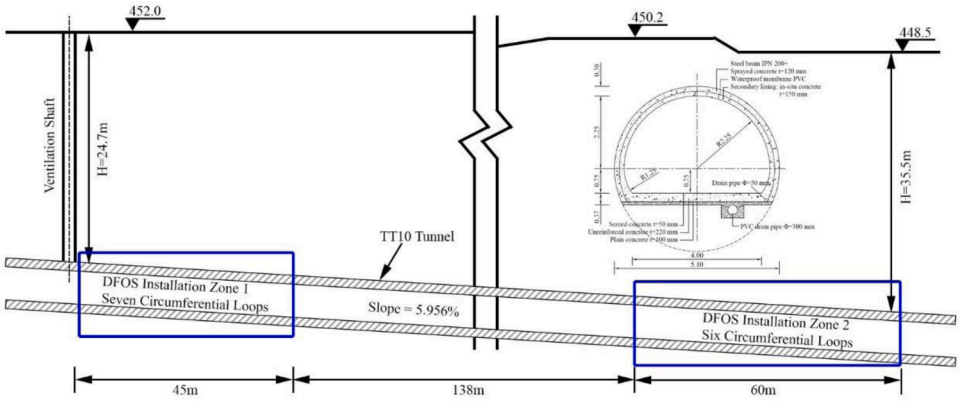


Fig. 9. Geodetic measurements for monitoring profile P0.

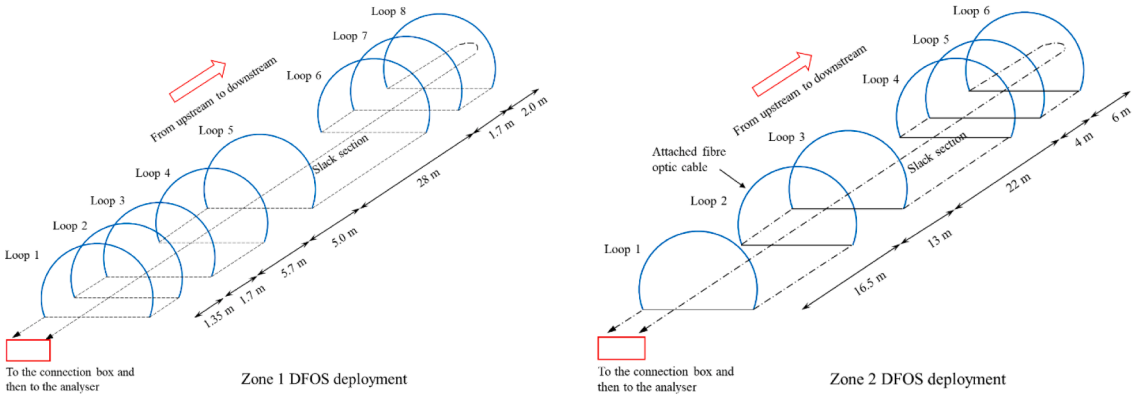
circumferential loops while the second zone involves 6 circumferential loops, as illustrated in 10(*b*). Sensing cables were attached to the tunnel liner using a hook-and-pully system with ten fixing points symmetrically placed along the circumference with an interval of around 0.8 m between two fixing points, as shown in Fig. 10(*c*). A three-year monitoring was conducted by Di Murro (2019) from 2014 to 2017, with strain readings taken every two-three months. The original monitoring data was presented in the raw form without processing. In a previous study, Xiao et al. (2024) applied a deconvolution procedure to derive the realistic strain for each gauge length and the corresponding tunnel convergence. This is because strain measurements collected by Brillouin optical time-domain analysis (BOTDA) represent a centrally weighted average over the spatial resolution of the analyser, meaning that strain readings near a fixing point can be influenced by the strain on the adjacent gauge lengths. This effect is particularly relevant here because the minimum spacing between fixing points is around 0.6 m (comparable to the BOTDA spatial resolution of 1.0 m). In the deconvolution method, the measured strain profile is modelled as the convolution of an underlying stepwise strain distribution between fixing points with a Gaussian weighting function representing the BOTDA response; the stepwise "actual" strains are then obtained by solving an optimisation problem that minimises the least-squares misfit between the measured strain profile and the reconstructed (re-convolved) profile. The recovered stepwise strains are subsequently integrated along each gauge length to compute tunnel convergence. This improves data quality by correcting for BOTDA spatial-averaging, thereby reducing cross-talk between adjacent gauge lengths and yielding more physically representative span-wise strains/convergence for subsequent comparison with the numerical model. More details of the monitoring and data processing can be found in Di Murro (2019) and Xiao et al. (2024). Due to the noise in the fibre optic data in zone 2, only readings from zone 1 were analysed. The DFOS loop 6 in the monitoring zone 1 corresponds to the Section 2 in the numerical model and the geodetic section P0. The tunnel convergence obtained from DFOS data before and after deconvolution (loop 6) is shown in Fig. 11.

4.2. *Numerical and field results comparison*

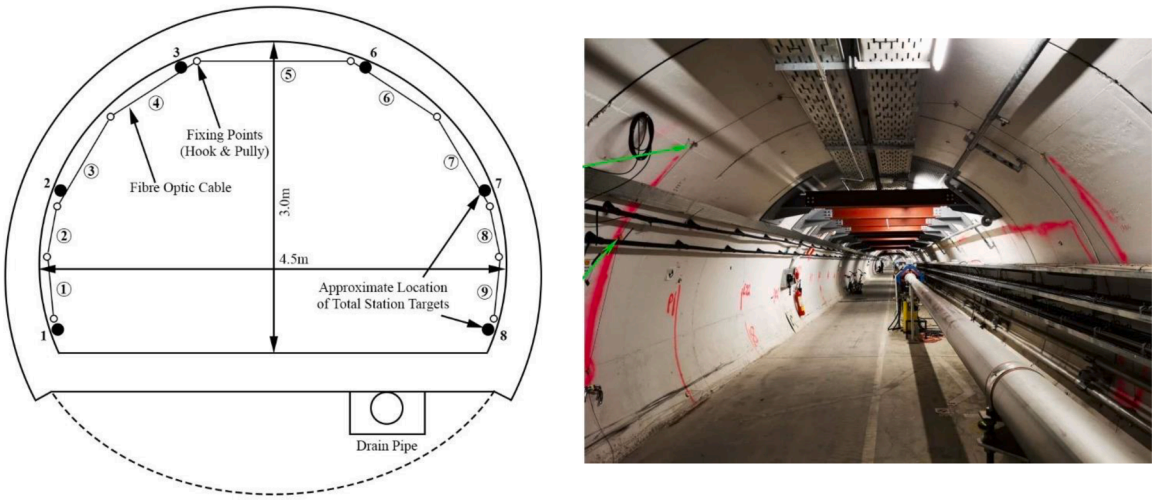
As the inclined tunnel traverses varying ground profiles and depths along its longitudinal direction, a representative tunnel cross-section is



(*a*) Two DFOS monitoring sections along TT10 tunnel (modified from Xiao et al. (2024))



(*b*) DFOS instrumentation layout in two zones along TT10 tunnel (Wang et al., 2024)



(*c*) Optic Fibre Cable Attachment with Gauge Numbering (modified from Xiao et al. (2024))

Fig. 10. Details of DFOS Monitoring along TT10 Tunnel.

selected for detailed investigation in this section (see Section 2 in Fig. 4). This cross-section is situated in the middle of the inclined tunnel model, with tunnel crown and tunnel axis level embedded in the weak marl layer while tunnel invert in the 2.1m-thick sandstone layer. It was selected as the representative numerical section because it coincides with the geodetic monitoring profile P0 and DFOS loop 6, allowing a direct spatial mapping between simulated outputs and field observations. In this study, the field datasets are used primarily for independent validation/interpretation of the simulated long-term response (rather than a formal inverse calibration), given the practical difficulty of uniquely back-analysing the time-dependent deterioration and swelling processes in an operational tunnel.

For geodetic comparison, nodal sets were defined in the FE model at locations corresponding to the geodetic targets (Fig. 8(b)). At each output time t, the deformed coordinates of target i are obtained as $x_i(t) = x_{i0} + u_i(t)$, and the distance between a monitored target pair (i, j) is computed as $d_{ij}(t) = ||x_i(t) - x_j(t)||$. The corresponding distance change is $\Delta d_{ij}(t) = d_{ij}(t) - d_{ij}(t_0)$, where t_0 is the baseline. The deformation rate for both field and numerical data is obtained as the slope of Δd_{ij} over the observation window (expressed in mm/year). For the DFOS comparison,

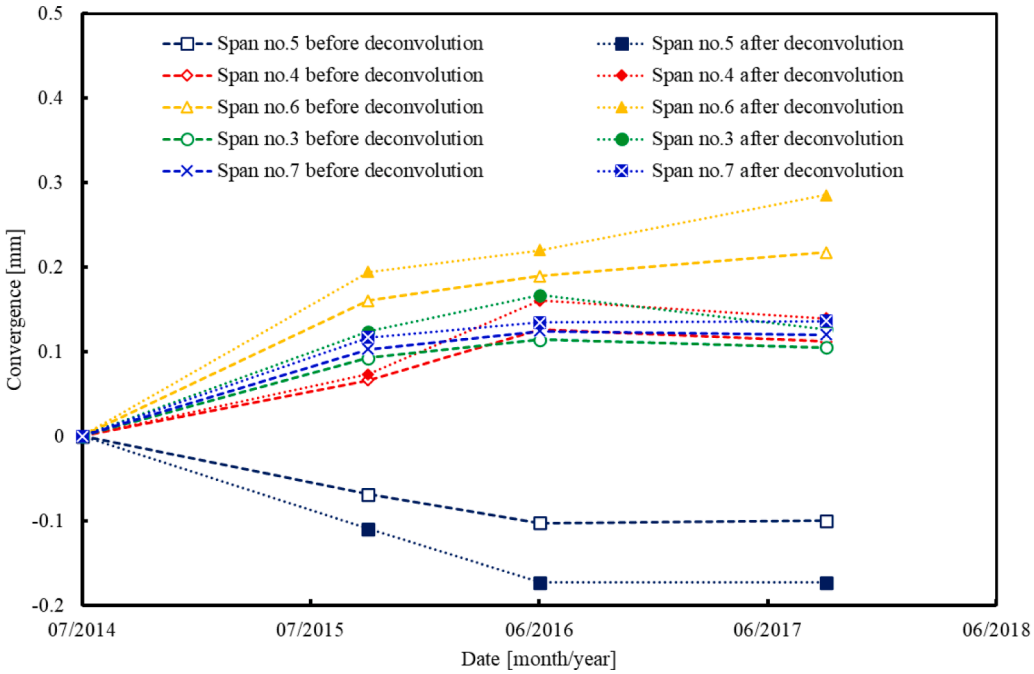
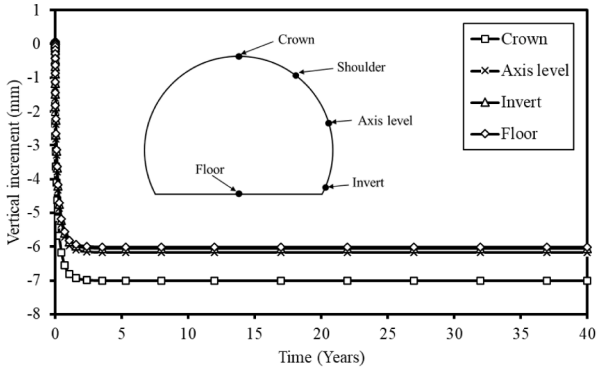
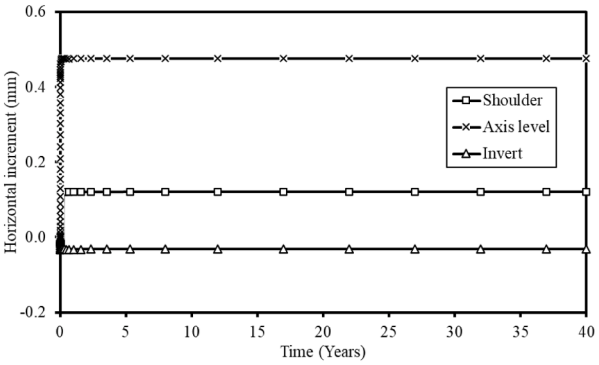


Fig. 11. Tunnel convergence converted from DFOS measurements.

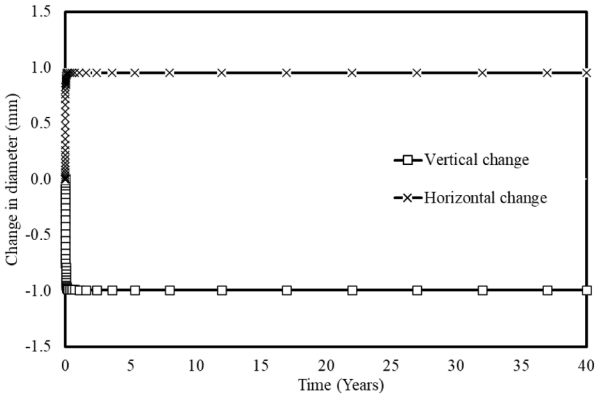
each gauge span corresponds to the chord length between two adjacent fixing points along the tunnel circumference (Fig. 10(c)). In the FE model, node sets were defined as the corresponding fixing-point locations, and the span length is computed as $L_s(t)=||x_a(t)- x_b(t)||$, where a and b are the two fixing points defining span s. The span change $\Delta L_s(t)= L_s(t)-L_s(t_0)$ is used to quantify extension/shrinkage, and the convergence rate is obtained as the slope of ΔL_s over time (mm/year). As the hydraulic/mechanical deterioration rates cannot be uniquely identified from field data, we adopt a bracketing validation strategy. For each mechanism/scenario, an UB and LB are defined to generate an envelope

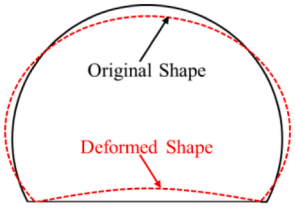


(*a*) Vertical incremental displacement



(*b*) Horizontal incremental displacement





(*c*) Change in tunnel diameter and tunnel deformation mode

Fig. 12. Incremental tunnel deformation during long-term operation stage.

of plausible responses. The model is considered to show satisfactory agreement if the field-derived deformation rates fall within the numerical UB-LB envelope, and the predicted deformation mode is consistent with the monitoring-derived deformation mode.

4.2.1. *Tunnel performance during long-term operation*

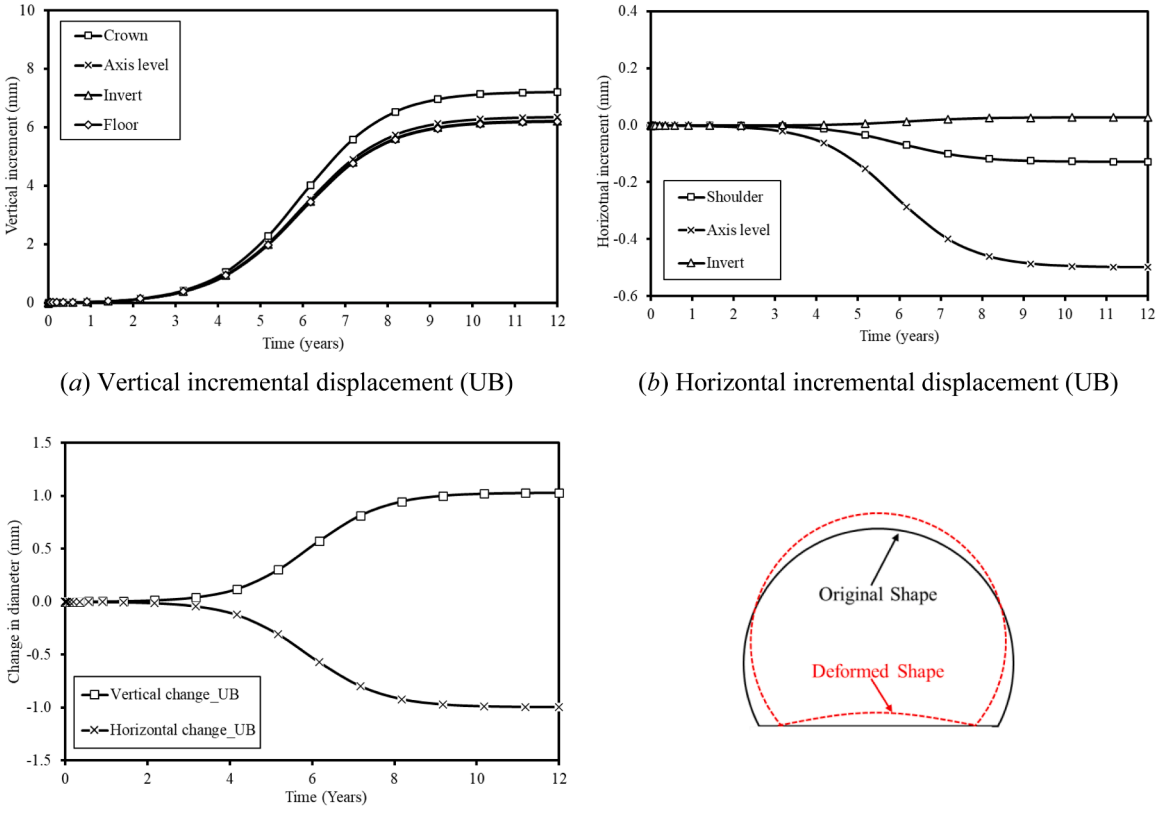
Fig. 12 shows the incremental displacement along tunnel Section 2 and the change in tunnel diameter with time during the long-term operation stage. As the ground consolidates, the vertical diameter of tunnel lining (i.e., the vertical displacement change between the tunnel crown and invert for this non-circular tunnel) decreases by 0.95 mm, which is accompanied by an increase of 0.95 mm in the horizontal diameter at tunnel axis level at the steady state, indicating a squatting deformation mode during this stage. Most of the tunnel squatting builds up within the first 2 years after construction as the ground around the tunnel gradually reaches a new steady-state flow condition.

4.2.2. *Tunnel performance subject to tunnel deterioration*

4.2.2.1. Effect of tunnel hydraulic deterioration. To investigate how lining hydraulic deterioration (HD) influences the aging performance of this tunnel section, the results of the upper bound are presented. Fig. 13 shows the development of vertical and horizontal displacement at the selected geodetic locations along the cross-section during hydraulic deterioration stage for the upper bound.

Fig. 13 shows that as a result of hydraulic deterioration, the tunnel undergoes relative movement with respect to the surrounding ground in both vertical and horizontal directions. Fig. 13(*a*) presents the development of incremental vertical displacement at the selected tunnel cross-section. The tunnel gradually shifts upward with a similar magnitude and rate at the crown, axis level, invert, and floor. This uniform upward movement suggests that the tunnel experiences a quasi-uniform displacement field, driven by the buoyancy effect induced by increasing pore water pressure around the tunnel due to decreasing drainage capacity. Similarly, the incremental horizontal displacement is shown in Fig. 13(*b*), where negative values indicate gradual tunnel convergence. The tunnel lining moves inward at shoulder and axis level, while the invert exhibits the slightest displacement. This deformation pattern due to hydraulic deterioration is entirely opposite to the long-term squatting deformation observed during the long-term operation stage (Fig. 12(*c*)). Beyond its relative movement, the tunnel also experiences internal deformation during the hydraulic deterioration stage. Fig. 13(*c*) shows an increase in tunnel diameter in the vertical direction and a reduction in the horizontal direction (i.e., a decrease in the distance at the tunnel axis level). This indicates that the tunnel lining deforms in a vertical elongation mode. The computed results align well with field observations, where cracks appear at the tunnel crown, accompanied by significant heaving at the tunnel floor and invert shown in Fig. 2. Noticeably, this deformation mode in Fig. 13(*d*) differs completely from the typical long-term squatting deformation commonly observed in aging segmental linings (Li et al., 2015; Wongsaroj et al., 2007). In conventional segmental tunnels, an initially watertight lining becomes increasingly permeable over time due to localised leakage at segmental joints. In contrast, the CERN TT10 tunnel, which was initially permeable, becomes relatively impermeable due to blocked drainage. This opposite change in lining permeability leads to significantly different long-term pore water pressure distributions and, consequently, distinct tunnel deformation modes.

In addition, Fig. 14 shows the development of the convergence between different DFOS monitoring spans, as shown in Fig. 10(*c*), in the upper bound case. It is clear in Fig. 14 that span 5 experienced shrinkage during the hydraulic deterioration stage while the two four spans, span 3/7 and span 4/6, were all observed to extend, indicating a similar deformation mode of vertical elongation (Fig. 13(*d*)).



(*a*) Vertical incremental displacement (UB)

(*b*) Horizontal incremental displacement (UB)

(*c*) Change in tunnel diameter (UB)

(*d*) Tunnel deformation mode (UB)

Fig. 13. Incremental tunnel deformation at geodetic locations during hydraulic deterioration.

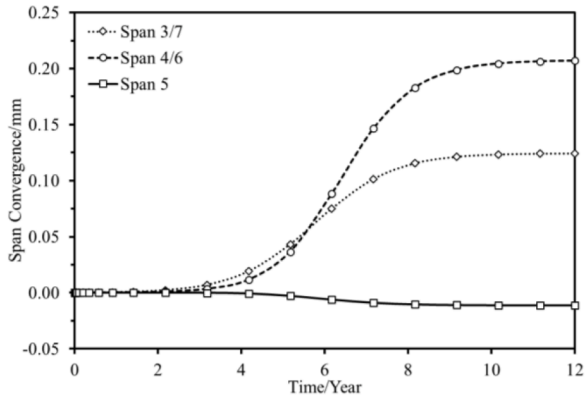


Fig. 14. Incremental tunnel deformation at DFOS spans during hydraulic deterioration.

To validate the numerical results against field measurements, the deformation rate of the distance change between monitoring points and the convergence rate between the gauge lengths, as shown in Fig. 8(*b*) and Fig. 10(*c*), are selected as the key indexes (Wang et al., 2024). Given that the hydraulic deterioration modelled in this paper occurs within a specific range, the numerical results are considered valid if the monitored deformation/convergence rate falls within the range of rates obtained from numerical studies with the upper and lower bound. Due to model symmetry, the deformation rates/convergence rates for monitoring distances 1–3 and 6–8 and gauge lengths 4/6 and 3/7 are identical in numerical simulations. Table 4 and 5 and Fig. 15 present a comparison of the deformation and convergence rates derived from numerical studies on the effect of hydraulic deterioration with those observed from both geodetic and DFOS monitoring, respectively.

It is clear to see from Table 4 that the maximum tunnel deformation rate among the four monitored distances affected by hydraulic deterioration is lower than the rate observed in field measurements except 1–3. However, the deformation mode induced by hydraulic deterioration shows consistency with the monitored deformation mode. Similarly, Table 5 shows that the maximum numerical rates of deformation at the five gauge-lengths all fall below the field rates at their corresponding length but the numerical deformation mode agrees with the field mode. Both comparisons suggest that hydraulic deterioration has a limited influence on the tunnel's long-term deformation. Therefore, it is essential to explore other contributing factors. The next section examines the impact of tunnel mechanical deterioration.

4.2.2.2. Effect of tunnel mechanical deterioration. In addition to hydraulic deterioration, tunnel mechanical deterioration (MD) is also modelled. Fig. 16 illustrates the development of horizontal and vertical displacements, as well as the changes in tunnel diameter over time during mechanical deterioration at the selected geodetic locations along the tunnel cross-section. Fig. 16(*a*) shows that tunnel crown is moving in an opposite direction to tunnel invert and floor, while Fig. 16(*b*) demonstrates tunnel axis is being squeezed towards tunnel interior. Compared to hydraulic deterioration, the tunnel lining exhibits inward deformation (i.e., contraction) due to the progressive reduction in its stiffness. As the deterioration of concrete lining continues, both the vertical and horizontal diameters decrease in an approximately linear manner over time, as shown in Fig. 16(*c*). This degradation leads to an inward convergence of tunnel lining in a nearly isotropic fashion illustrated in Fig. 16(*d*).

Table 4
Numerical and geodetic deformation rates comparison under hydraulic deterioration.

Deterioration	Scenarios	Deformation rate between geodetic monitoring locations (mm/year)			
		Distance 1–3	Distance 1–8	Distance 3–6	Distance 2–7
Hydraulic	Numerical-UB	0.007	−0.034	−0.063	−0.140
	Numerical-LB	0.0002	−0.002	−0.004	−0.009
Field	Geodetic Rate	0.002	−0.048	−0.147	−0.299

Note: The negative value means the distance between the points is decreasing and vice versa.

Table 5
Numerical and DFOS convergence rates comparison under hydraulic deterioration.

Scenarios		Convergence rate between DFOS monitoring spans (mm/year)				
		Span 5	Span 4	Span 6	Span 3	Span 7
HD	UB	−0.0009	0.0172	0.0172	0.0103	0.0103
	LB	−0.00004	0.0010	0.0010	0.0014	0.0014
Field	DFOS (deconvoluted)	−0.0532	0.0676	0.0493	0.0390	0.0413

Note: The negative value means the distance between the points is decreasing and vice versa.

Similarly, Fig. 17 presents the development of the convergence between different DFOS monitoring spans under mechanical deterioration of the upper bound case. It is evident that all spans experienced shrinkage during the hydraulic deterioration stage, suggesting a contraction of the tunnel section (Fig. 16(*d*)).

To understand the effect of tunnel mechanical deterioration, the rates of deformation and convergence obtained from the modelling of mechanical deterioration are compared against the field geodetic and DFOS measurements in Tables 6 and 7 and Fig. 18, respectively.

Table 6 and Fig. 18 show that the field rates at locations 3–6 and 2–7 are bigger than the numerical rates at the corresponding locations while the field rate at location 1–8 falls within the numerical rate range. However, for location 1–3, the rate is smaller than the rate obtained from the lower bound and the direction of the deformation is the opposite. The results showed that the deformation mode derived from modelling mechanical deterioration differs from the mode captured from field monitoring and the deformation rates do not agree with field rates. Similarly, the comparison between numerical results and DFOS results in Table 7 and Fig. 18 shows that the maximum numerical rate of deformation for spans 5 and 4/6 is smaller than the field rate at these locations whilst the field deformation rate at spans 3/7 falls within the obtained numerical range for this span. It is worthy of noting that the almost isotropic contraction mode obtained from numerical simulations poses a stark contrast to the elongation mode observed in field monitoring. Therefore, it is believed that tunnel mechanical deterioration, similar to hydraulic deterioration, is not the main contributing factor leading to the observed long-term tunnel deformation.

4.2.2.3. Effect of coupled hydromechanical deterioration. In practice, the above two tunnel deteriorations occur concurrently instead of individually and they occur in no specific order. In this regard, a new simulation subject to coupled hydromechanical deterioration (HMD) was conducted. The worst individual deterioration is coupled as the upper bound and the least individual deterioration is modelled as the lower bound. Fig. 19 presents the lining deformation at the selected geodetic locations in two directions of the UB case with time.

The tunnel deformation is very small within the first 3–4 years and then starts to build up at a faster rate. Compared with the effect of individual deterioration in Figs. 13 and 16, the deformation pattern in Fig. 19 shows that hydraulic deterioration dominates the tunnel deformation in the vertical direction (Fig. 13(*a*) and Figure 19(*a*)) while mechanical degradation contributes mostly to the horizontal

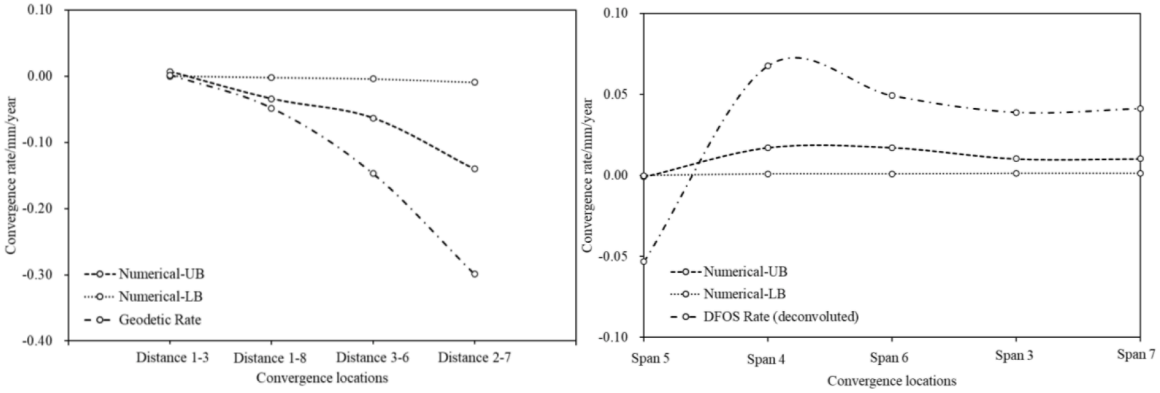
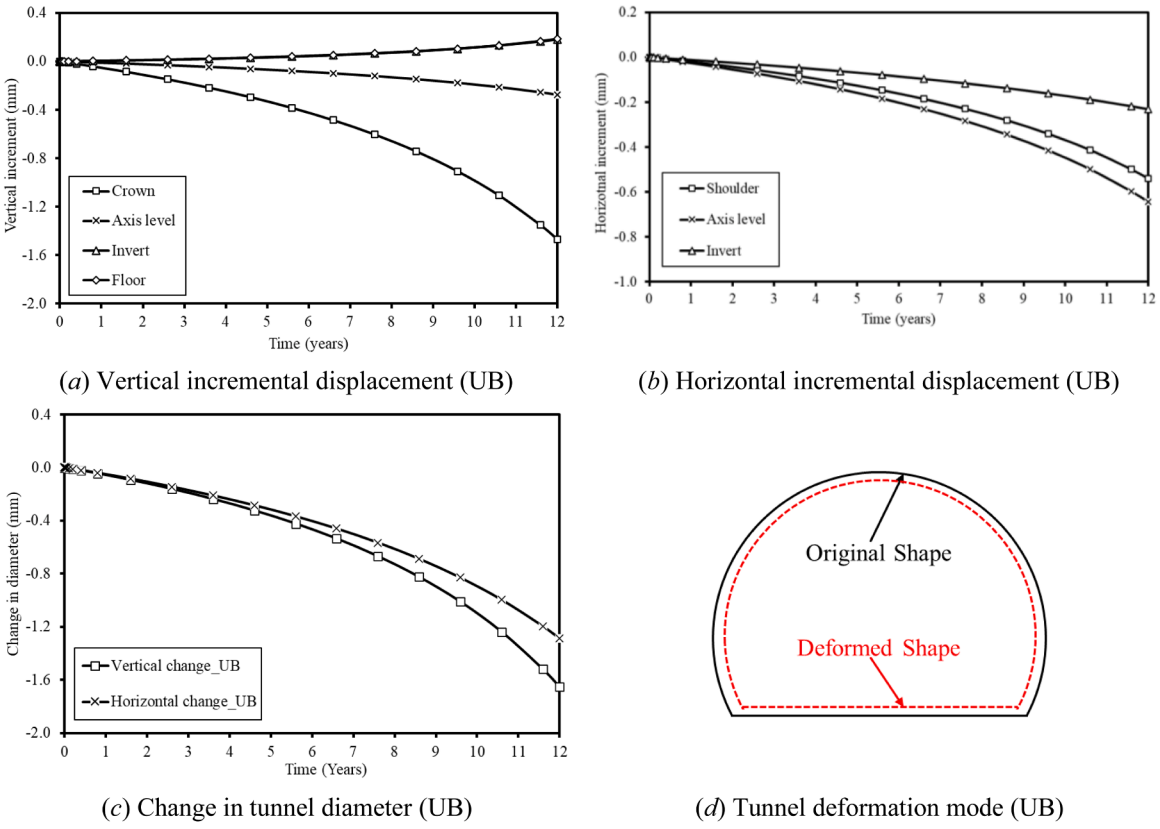


Fig. 15. Comparison between numerical and field deformation rates under hydraulic deterioration.



(*a*) Vertical incremental displacement (UB)

(*b*) Horizontal incremental displacement (UB)

(*c*) Change in tunnel diameter (UB)

(*d*) Tunnel deformation mode (UB)

Fig. 16. Incremental tunnel deformation at geodetic locations during mechanical deterioration.

deformation (Figs. 16(*b*) and 19(*b*)). In the UB case where the tunnel experiences the worst hydraulic and mechanical deterioration, the tunnel experienced vertical elongation during year 4–8 while exhibited contraction for the remaining years, indicating the contributions of two deteriorations to the lining deformation in this case are unequal, in which the hydraulic deterioration prevails in the time period of 4 to 8 years and structural deterioration dominates thereafter. This is due to the fact that the decrease of lining permeability would significantly affect the tunnel deformation at the beginning, then the further decrease just has slight effect after the almost fully clogging condition reaches. In terms of the magnitude of the deformation, such coupling indeed induced greater deformation than each individual deterioration did. Additionally, Fig. 20 shows the development of the convergence between different DFOS monitoring spans subject to coupled hydromechanical deterioration of the UB case. Clearly, Fig. 20 shows an increasing trend for span 4/6 and span 3/7 but a decreasing trend for span 5, demonstrating a deformation mode of vertical elongation that is in agreement with field observation and also Figure 13(*b*).

To compare the tunnel performance subject to the coupled hydro-mechanical deterioration, Tables 8 and 9 and Fig. 21 present the rate of deformation and convergence obtained from numerical simulations and field geodetic and DFOS monitoring, respectively.

Table 8 and Fig. 21 reveal that, similar to mechanical deterioration, the field deformation rate at locations 3–6 and 2–7 exceeds the corresponding numerical rate, while at location 1–8, it falls within the numerical range. However, at location 1–3, the field rate is lower than the numerical lower bound, and the deformation direction is opposite. Similarly, the comparison between numerical results and DFOS results in Table 9 and Fig. 21 shows that the maximum numerical rate of deformation for span 3/7 and span 4 is smaller than the field rate at these locations whilst the field deformation rate at span 5 and span 6 falls within the obtained numerical range. The numerical deformation

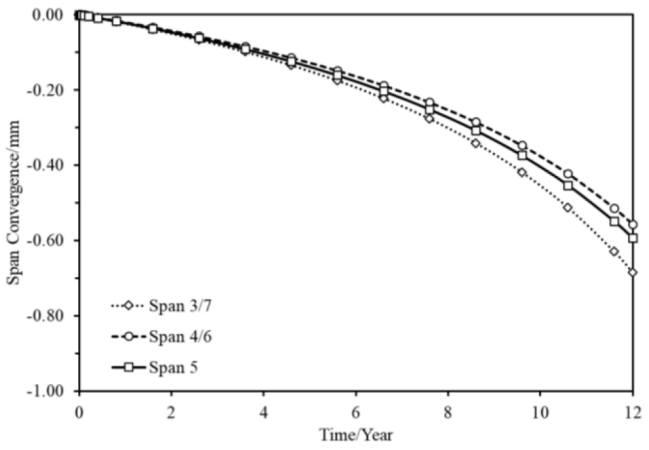


Fig. 17. Incremental tunnel convergence at DFOS spans during mechanical deterioration.

Table 6
Numerical and field deformation rates comparison under mechanical deterioration.

Deterioration	Scenarios	Deformation Rate between Monitoring Locations (mm/year)			
		Distance 1–3	Distance 1–8	Distance 3–6	Distance 2–7
Mechanical	Numerical-UB	−0.039	−0.090	−0.107	−0.119
	Numerical-LB	−0.010	−0.019	−0.024	−0.025
	Field Rate	0.002	−0.048	−0.147	−0.299

Note: The negative value means the distance between the points is decreasing and vice versa.

mode also shows is consistent with the mode observed from DFOS monitoring. Overall, the simulated deformation rate from coupled hydromechanical deterioration remains in consistent with the observed field rate in this coupled hydromechanical deterioration, suggesting there are additional contributing factors to tunnel deformation. The results also indicate that coupled deterioration primarily affects the tunnel's upper section, while the lower section experiences less deformation. This discrepancy may be attributed to the layered ground composition, where the upper section is embedded in swelling marl, while the lower section rests in sandstone. The next section investigates the impact of the swelling marl ground layer.

4.2.3. *Tunnel performance subject to marl swelling*

As mentioned in Section 3.5, the swelling behaviour of the marl layer should be considered to account for the ongoing TT10 tunnel deformation. Based on the CERN tunnel rock creep test data, a series of numerical simulations were conducted to investigate the coupled effect of the swelling marl and hydromechanical deterioration on the long-term ageing performance of the TT10 tunnel. The upper and lower bound of this simulation assumes the same upper and lower bound of the coupled hydromechanical deterioration. Fig. 22 presents the development of lining deformation of the upper bound at selected geodetic location of Section 2 of the numerical model in this situation.

Fig. 22 illustrates that tunnel deformation due to coupled marl swelling and hydromechanical deterioration is significantly greater than that caused by individual hydraulic and mechanical deterioration, or their coupled hydromechanical effect, as shown in Figs. 13, 16, and 19. Similarly, Fig. 23 shows the development of the convergence between different DFOS monitoring spans subject to coupled marl swelling and hydromechanical deterioration of the UB case. Like Fig. 20, it shows an increasing trend for span 4/6 and span 3/7 but a decreasing trend for span 5 but with a bigger magnitude, suggesting that the coupling of marl swelling contributes to bigger tunnel deformation. Compared to coupled hydromechanical deterioration, the inclusion of marl swelling leads to further tunnel contraction both horizontally and vertically, but with smaller contraction in the vertical direction, enabling a similar elongated contraction mode as in Fig. 19(*d*).

To assess tunnel performance under the combined effects of marl swelling and hydromechanical deterioration, Tables 10 and 11 and Fig. 24 compare the deformation and convergence rates obtained from

Table 7
Numerical and DFOS convergence rates comparison under mechanical deterioration.

Scenarios		Convergence rate between monitoring spans (mm/year)				
		Span 5	Span 4	Span 6	Span 3	Span 7
MD	UB	−0.0494	−0.0464	−0.0464	−0.0571	−0.0571
	LB	−0.0109	−0.0101	−0.0101	−0.0118	−0.0118
Field	DFOS (deconvoluted)	−0.0532	0.0676	0.0493	0.0390	0.0413

Note: The negative value means the distance between the points is decreasing and vice versa.

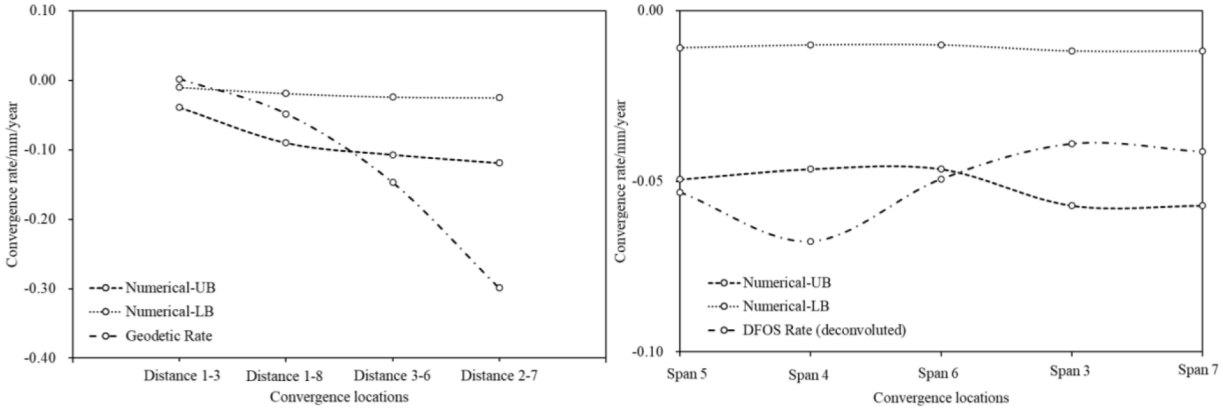
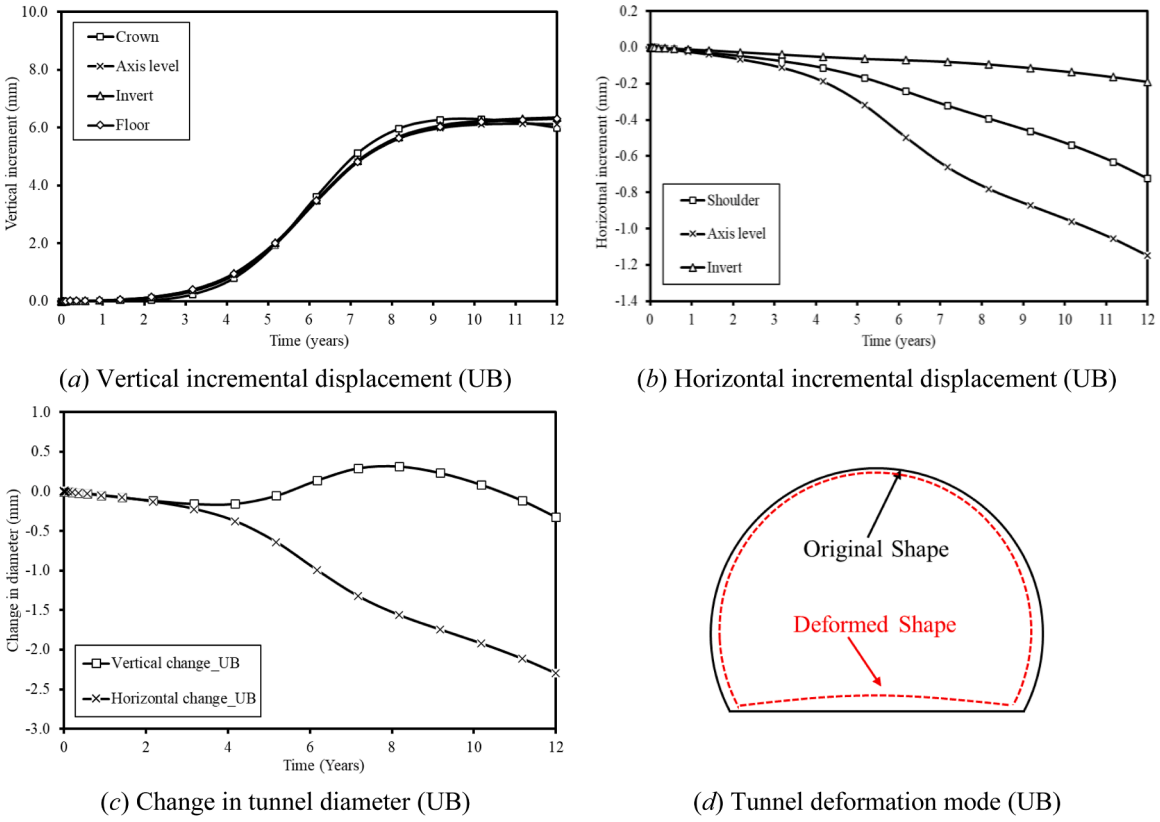


Fig. 18. Comparison between numerical and field deformation rates under mechanical deterioration.



(*a*) Vertical incremental displacement (UB)

(*b*) Horizontal incremental displacement (UB)

(*c*) Change in tunnel diameter (UB)

(*d*) Tunnel deformation mode (UB)

Fig. 19. Incremental tunnel deformation at geodetic locations during coupled hydromechanical deterioration.

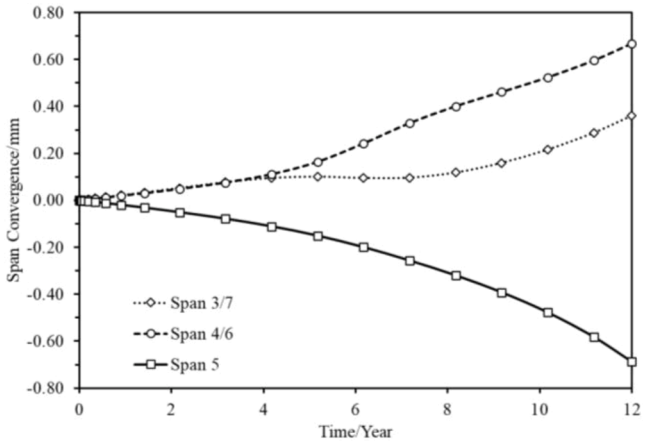


Fig. 20. Incremental tunnel convergence at DFOS spans during hydromechanical deterioration.

numerical simulations and field measurements, respectively.

The comparison in Table 10 and Fig. 24 shows that the field deformation rates fall within the range predicted by numerical simulations of coupled marl swelling and hydromechanical deterioration, except for direction of the deformation between distance 1–3. This discrepancy is likely attributable to a combination of (1) the discrete nature of the geodetic dataset, which may not fully represent the deformation profile of the analysed section, and (2) site-specific geological or structural variations (spatial heterogeneity of the surrounding ground or unmodelled weak zones) that are not fully considered by the homogenised ground representation adopted in the model. Further work with more detailed ground characterisation and related modelling would be required to specifically examine the influence of these factors. However,

Table 9
Numerical and DFOS convergence rates comparison under hydromechanical deterioration.

Scenarios		Convergence rate between monitoring spans (mm/year)				
		Span 5	Span 4	Span 6	Span 3	Span 7
HMD	UB	−0.0572	0.0557	0.0557	0.0301	0.0301
	LB	−0.0110	0.0107	0.0107	0.0101	0.0101
Field	DFOS (deconvoluted)	−0.0532	0.0676	0.0493	0.0390	0.0413

Note: The negative value means the distance between the points is decreasing and vice versa.

Table 8
Numerical and field deformation rates comparison under hydromechanical deterioration.

Deterioration	Scenarios	Deformation Rate between Monitoring Locations (mm/year)			
		Distance 1–3	Distance 1–8	Distance 3–6	Distance 2–7
Hydromechanical	Numerical-UB	−0.032	−0.058	−0.121	−0.192
	Numerical-LB	−0.011	−0.020	−0.022	−0.034
	Field Rate	0.002	−0.048	−0.147	−0.299

Note: The negative value means the distance between the points is decreasing and vice versa.

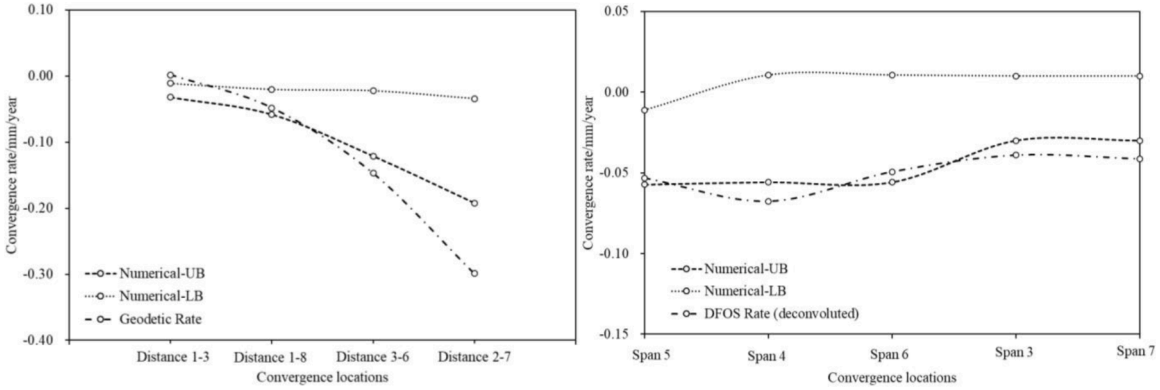
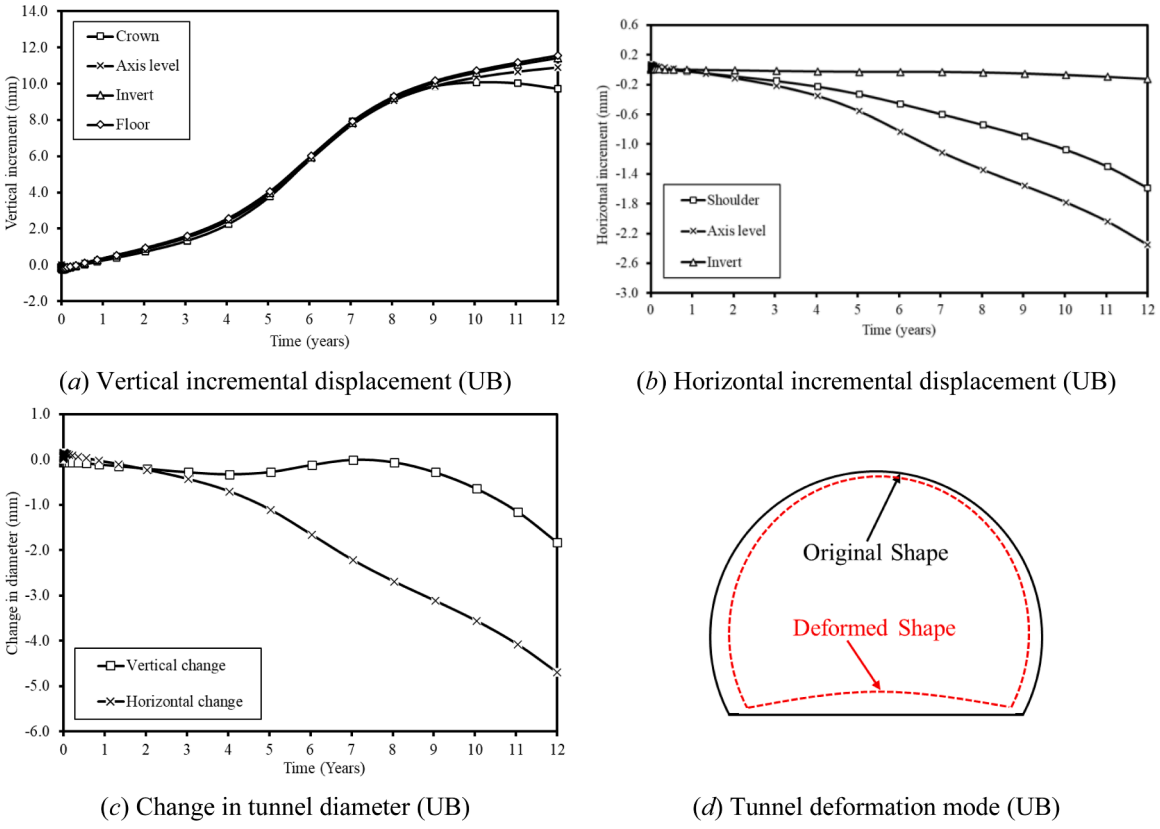


Fig. 21. Comparison between numerical and field deformation rates under hydromechanical deterioration.



(*a*) Vertical incremental displacement (UB)

(*b*) Horizontal incremental displacement (UB)

(*c*) Change in tunnel diameter (UB)

(*d*) Tunnel deformation mode (UB)

Fig. 22. Incremental tunnel deformation at geodetic locations subject to coupled marl swelling and tunnel hydromechanical deterioration.

the comparison between numerical results and DFOS results in Table 11 and Fig. 24 shows that the field DFOS rates of deformation fall within the range of deformation rates obtained from simulating the coupled effect of marl swelling and hydromechanical deterioration. The numerical deformation mode also is consistent with the mode observed from DFOS monitoring. The underlying mechanism behind the swelling effect of the marl layer lies in the volume expansion of the marl when exposed to groundwater. The clogging of the tunnel drainage system leads to the accumulation of pore water pressure behind the tunnel lining, and this causes the clay minerals in the marl layer to absorb water, contributing to the swelling of the marl layer. With time, the swelling pressure induces the volume expansion of the marl and additional stresses on tunnel linings and surrounding rock masses, leading to progressive deformations in tunnel linings. Based on these findings, it is reasonable to conclude (1) the numerical model is examined through the agreement between the field deformation rates and the numerical results, and (2) marl swelling is the primary factor driving the long-term tunnel deformation, while hydraulic and mechanical deterioration have a less significant influence.

5. Parametric study

At CERN, over 70 km of ageing tunnels traverse a complex geological setting, with layered ground conditions exhibiting varying mechanical and hydraulic properties along their length. This section explores the impact of ground layering and ground permeability anisotropy on tunnel deformation, aiming to provide a comprehensive understanding of the diverse behaviours across different sections of this large-scale underground infrastructure.

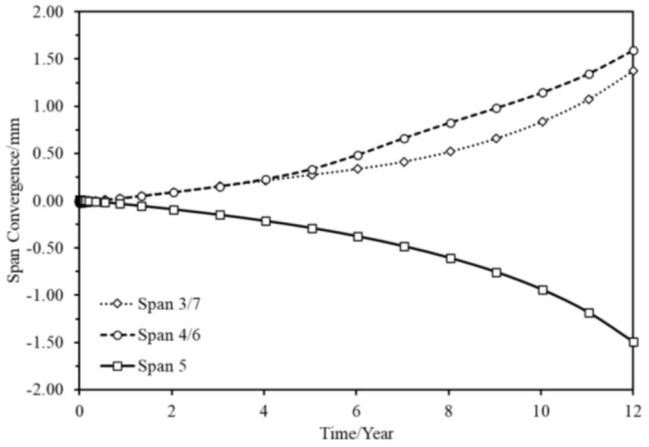


Fig. 23. Incremental tunnel convergence at DFOS spans subject to coupled marl swelling and tunnel hydromechanical deterioration.

5.1. *Effect of ground layering on tunnel behaviour*

In addition to the previously discussed tunnel Section 2, the parametric study examines two additional tunnel cross-sections, Sections 1 and 3, representing the ground conditions around the inclined CERN tunnel at different depths (Fig. 4). Section 1, entirely embedded in a weak marl layer at a depth of 24 m, contrasts with Section 3, which lies at 31 m depth, where the tunnel crown is in the sandstone unit, the invert in the weak marl unit, and a sandy marl interlayer in between (Fig. 4(*b*)).

Figure 25(*a*) presents the tunnel diameter change during hydraulic deterioration, showing a consistent deformation pattern in Sections 1, 2 and 3 - vertical elongation due to an increase in vertical diameter and a decrease in horizontal diameter. However, when the ground permeability anisotropy is not considered, Section 3 exhibits an opposite deformation mode, with horizontal expansion and slight vertical contraction, resulting in a subtle squatting deformation mode (Fig. 25 (*b*)). These findings highlight that it is highly important to consider the significant effect of ground permeability anisotropy on the long-term tunnel deformation.

Fig. 26 compares the normalised pore water pressure distribution around the tunnel circumference for the three selected cross-sections when $RP = 0.1$. In Section 1, where the tunnel is entirely embedded in marl, the normalised pore water pressure gradually decreases along the tunnel circumference from the crown to the axis level as the tunnel elongates vertically. Compared to the upper tunnel section above the invert, the pore water pressure at the tunnel floor is lower, as the floor experiences significantly greater heave than horizontal convergence, similar to the behaviour observed in Section 2. In Section 3, where the tunnel is embedded in a layered ground, the permeability of the upper layer (sandstone) is an order of magnitude higher than that of the lower layers (marl and sandy marl), which is the opposite of the conditions in Section 2. Consequently, unlike in Section 2, the normalised pore water pressure in the lower ground layer beneath the tunnel shoulder ($\theta < 30°$) is significantly lower than in the upper layer. This comparison highlights the combined effects of non-circular tunnel geometry and layered

Table 10
Deformation rates comparison under coupled marl swelling and hydromechanical deterioration.

Deterioration	Scenarios	Deformation Rate between Monitoring Locations (mm/year)			
		Distance 1–3	Distance 1–8	Distance 3–6	Distance 2–7
Coupled marl swelling and hydromechanical deterioration	Numerical-UB	−0.021	−0.194	−0.265	−0.391
	Numerical-LB	−0.001	−0.037	−0.070	−0.106
	Field Rate	0.002	−0.048	−0.147	−0.299

Note: The negative value means the distance between the points is decreasing and vice versa.

Table 11
Numerical and DFOS convergence rates comparison under coupled marl swelling and hydromechanical deterioration.

Scenarios		Convergence rate between monitoring spans (mm/year)				
		Span 5	Span 4	Span 6	Span 3	Span 7
HMDCREEP	UB	−0.1243	0.1326	0.1326	0.1146	0.1146
	LB	−0.0311	0.0367	0.0367	0.0372	0.0372
Field	DFOS (deconvoluted)	−0.0532	0.0676	0.0493	0.0390	0.0413

Note: The negative value means the distance between the points is decreasing and vice versa.

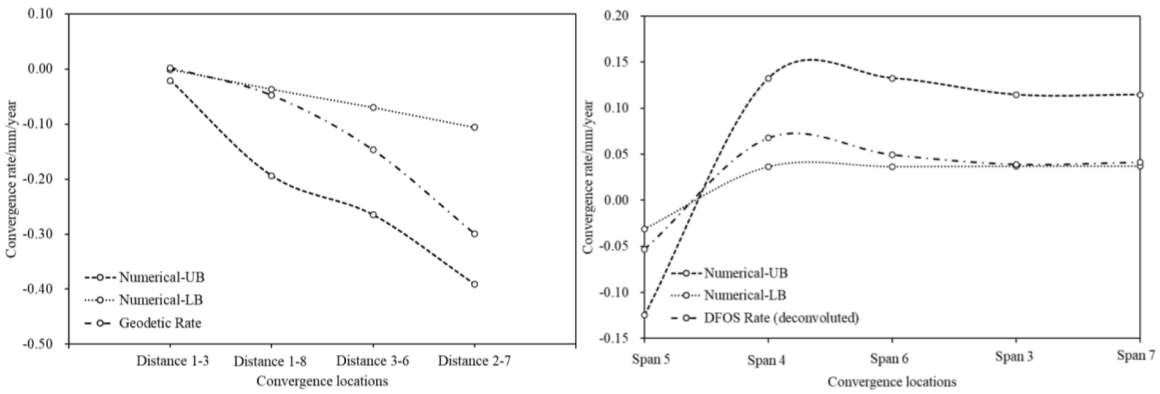
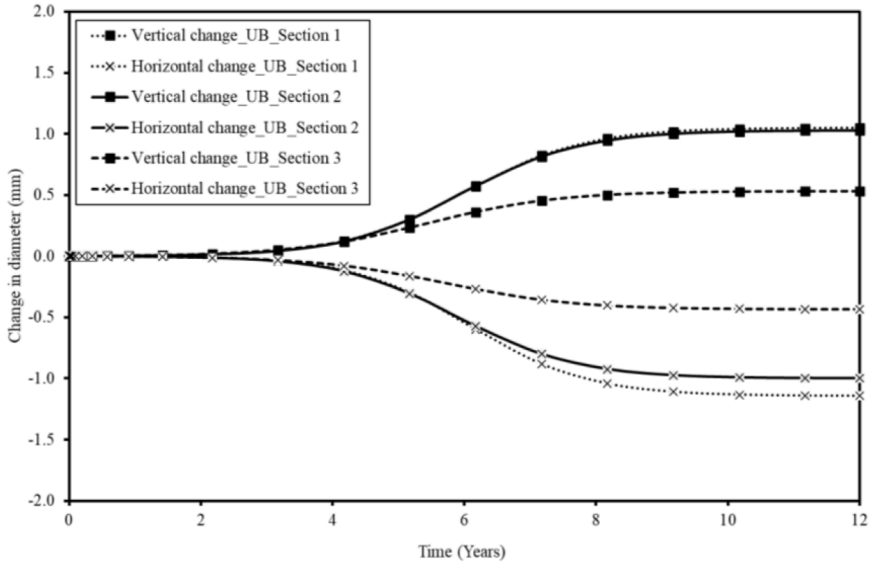
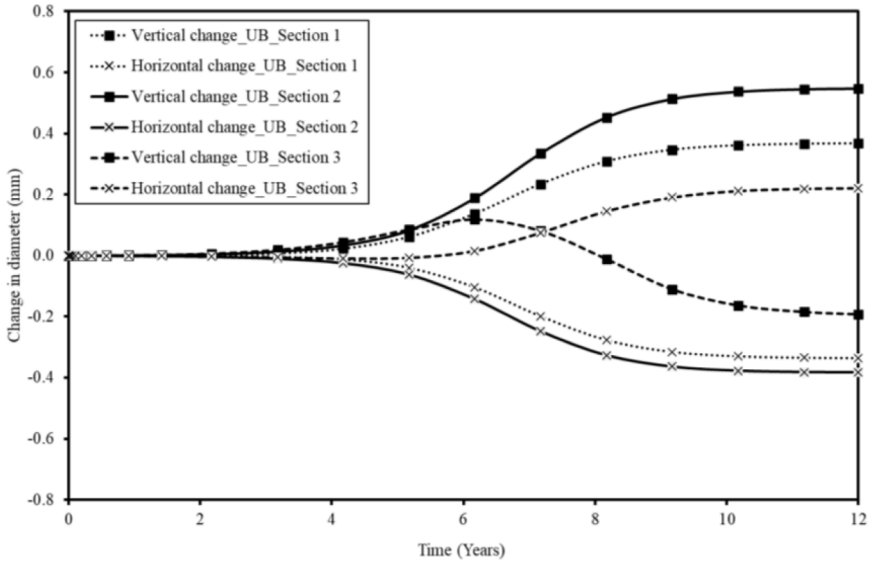


Fig. 24. Comparison between numerical and field deformation rates under coupled marl swelling and hydromechanical deterioration.



(*a*) with ground permeability anisotropy (k_h/k_v=10)



(*b*) without ground permeability anisotropy

Fig. 25. Change in tunnel diameter during hydraulic deterioration for the three tunnel cross-sections.

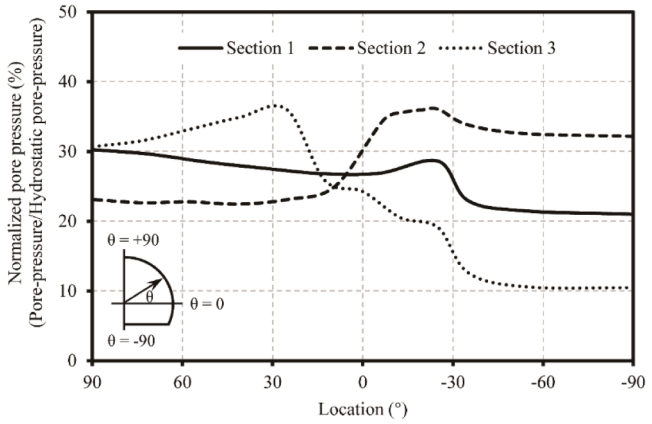


Fig. 26. Comparison of normalised pore water pressure distributions for the three tunnel cross-sections.

ground conditions on pore water pressure distribution around the tunnel lining.

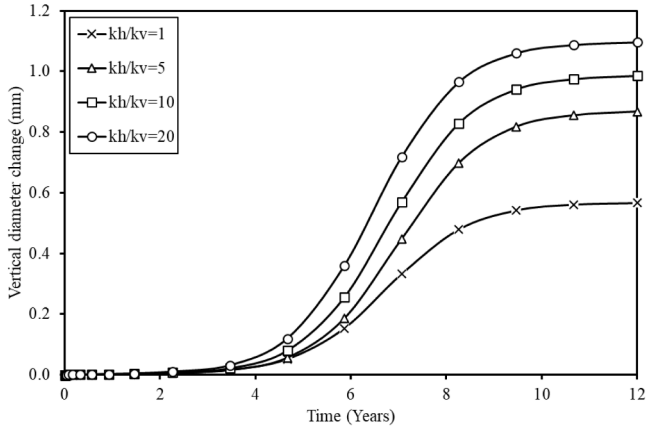
5.2. *Effect of ground permeability anisotropy on tunnel response*

As discussed above, ground permeability significantly influences the magnitude and distribution of pore water pressure around the tunnel circumference, affecting tunnel deformation. To assess the impact of permeability anisotropy, a parametric study was conducted at the hydraulic deterioration stage, keeping the vertical permeability (k_v) constant while varying the horizontal-to-vertical permeability ratio (k_h/k_v) from 1 (isotropic) to 5, 10, and 20 of the marl layer in Figure 4(*a*). FE results indicate that the final pore pressure acting on the lining remains largely unaffected by permeability anisotropy when assuming a fully permeable lining during long-term operation and a fully impermeable lining during hydraulic deterioration. However, as shown in Fig. 27, permeability anisotropy significantly affects tunnel deformation. Using the tunnel Section 2 as an example, increasing k_h/k_v leads to notable

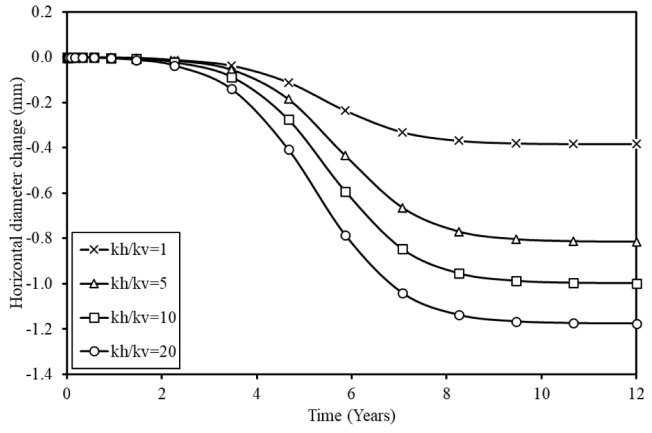
changes in tunnel diameter in both vertical and horizontal directions during hydraulic deterioration. The results suggest that higher permeability anisotropy amplifies vertical elongation and horizontal contraction of the tunnel as it alters earth pressure distribution around the lining.

In the previous FE models, a uniform permeability anisotropy ratio was assumed for all units in the Molasse formation. However, in practice, this ratio varies across different ground layers. In the red Molasse, several interbedded units have been identified (see Fig. 3). To investigate the effect of permeability anisotropy of local layers on tunnel performance, Figure 28(*a*) and Figure 28(*b*) compare the tunnel diameter changes at Section 2 for three cases: (1) permeability anisotropy assumed for all units in Molasse (Case 1); (2) permeability anisotropy assumed for sandstone unit only (Case 2), and (3) no permeability anisotropy assumed (Case 3). The results indicate tunnel deformation in the second case falls between that of the first and third case, confirming the aforementioned finding that permeability anisotropy enhances the tunnel deformation. A similar trend is observed in Section 3.

In Section 1, although the tunnel is fully embedded in the Marl unit with an underlying sandstone layer, the permeability anisotropy of the sandstone alone significantly influences tunnel deformation (Case 2). Initially, it was expected that tunnel deformation in Case 2 would be similar to that in Case 3, given that the tunnel is situated above the sandstone. However, results show that deformation in Case 2 is greater than in Case 3, as illustrated in Figs. 28(*c*) and (*d*). This could be attributed to the 3D effect of tunnel deformation, where cross-sectional deformation is influenced by adjacent sections and ground-structure interactions along the tunnel's longitudinal direction. These findings emphasise the necessity of 3D modelling for tunnels passing through heterogeneous ground layers, as 2D models often fail to capture such critical effects. Moreover, they further highlight the importance of considering ground permeability anisotropy when assessing long-term tunnel responses under hydromechanical deterioration.



(*a*) vertical direction



(*b*) horizontal direction

Fig. 27. Change in tunnel diameter with various permeability anisotropy during hydraulic deterioration.

6. Conclusions

This study presents a series of three-dimensional hydromechanical coupled finite element analysis to evaluate the long-term ageing performance of the CERN TT10 tunnel. The impact of tunnel hydraulic deterioration, mechanical deterioration, and marl swelling was investigated, and the ranges of numerical deformation rates were compared against field geodetic and DFOS monitoring data, validating the numerical model. In addition, further parametric studies on the effect of ground layering and ground permeability anisotropy were also conducted. The findings provide new insights into the ageing performance of a non-circular tunnel embedded in changing three-dimensional ground profiles, and the main conclusions can be drawn as follows:

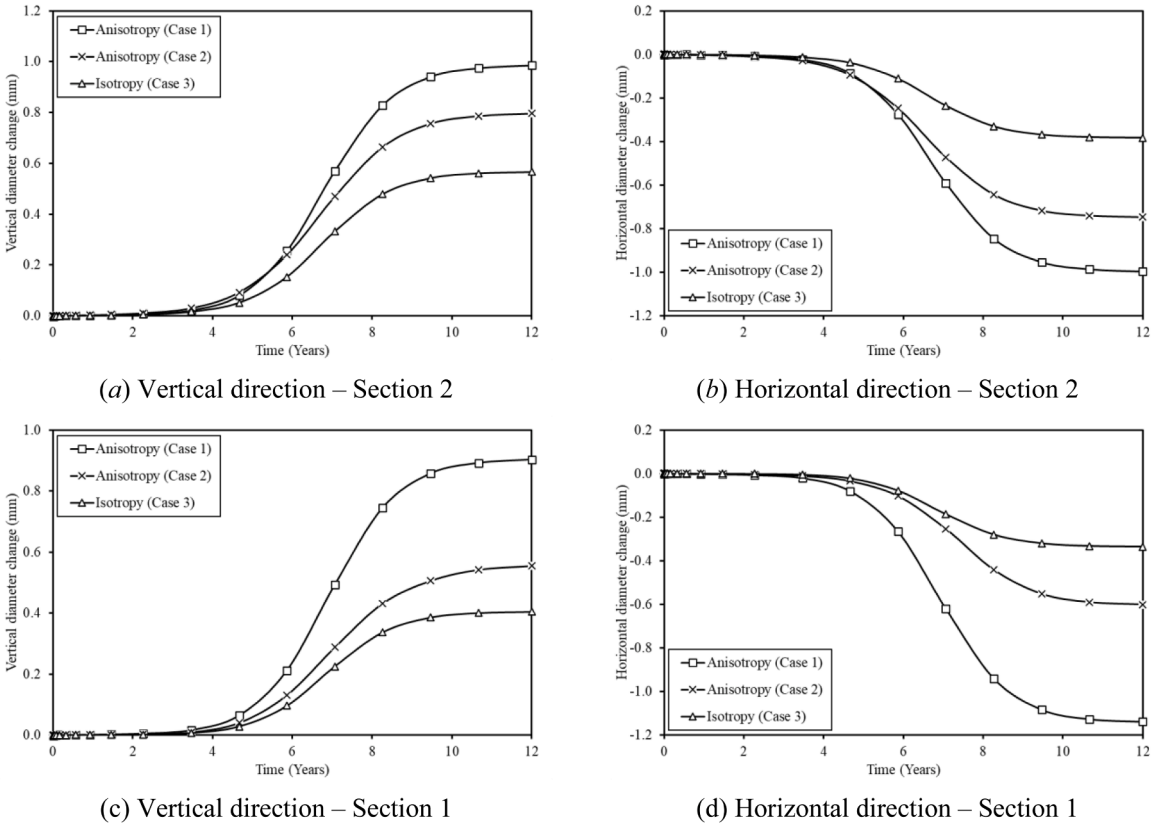
(1) During long-term operation, the tunnel initially experiences squatting deformation, with vertical displacement decreasing and horizontal displacement increasing as the ground consolidates. Most deformation occurs within the first two years. TT10′s long-term squatting deformation mode shifts to vertical elongation as drainage clogging increases pore water pressure.

(2) Hydraulic deterioration, caused by drainage system clogging, leads to the vertical elongation of the tunnel, whereas structural deterioration results in overall contraction. When coupled, hydraulic deterioration dominates tunnel deformation in the early years, while structural degradation-induced tunnel deformation becomes more significant over time. Their coupled effect leads to greater deformation than either mechanism alone. However, upon comparison with field measurements, both deteriorations only play a limited role in the tunnel's long-term performance.

(3) The swelling marl effect is the dominant factor in long-term tunnel deformation, exceeding the individual and combined effects of hydraulic and mechanical deterioration. Numerical results show that geodetic field deformation rates and DFOS convergence rates align with predictions from the coupled marl swelling and hydromechanical deterioration, with one exception for the deformation direction of geodetic distance 1–3. This discrepancy likely arises from the discrete nature of the geodetic data that fail to capture the comprehensive deformation profile of the tunnel section. Nevertheless, the FE results show agreement with the DFOS rates of convergence and mode of deformation because the field DFOS rates of convergence fall within the range of rates obtained from simulating the coupled effect of marl swelling and hydromechanical deterioration.

(4) The swelling marl effect is driven by groundwater-induced expansion of clay minerals within the marl layer. As the tunnel drainage system deteriorates, increased pore water pressure leads to water absorption by the marl, causing volumetric expansion. This swelling generates additional stresses on the tunnel lining and surrounding rock, leading to progressive tunnel contraction, floor heave, and lining cracking. Over time, these deformations accumulate, making groundwater control crucial for mitigating long-term tunnel ageing effects.

(5) The ground layering significantly influences tunnel deformation modes along its length. When ground permeability anisotropy is not considered, in marl-dominated Sections 1 and 2, the tunnel exhibits vertical elongation, whereas in Section 3 where the upper part is embedded in high-permeability sandstone and the lower part in low-permeability marl, a slight squatting deformation occurs. However, when permeability anisotropy is



(*a*) Vertical direction – Section 2 (*b*) Horizontal direction – Section 2

(c) Vertical direction – Section 1 (d) Horizontal direction – Section 1

Fig. 28. Change in tunnel diameter for Sections 2 and 1 with permeability anisotropy of various ground unit during hydraulic deterioration stage.

considered, vertical elongation becomes the dominant mode across all sections, aligning better with field measurements.

(6) Ground permeability anisotropy has a significant impact on tunnel deformation and pore water pressure distribution. The increase of permeability ratio leads to notable changes in tunnel diameter in both vertical and horizontal directions during hydraulic deterioration. The results suggest that higher permeability anisotropy amplifies vertical elongation and horizontal contraction of the tunnel as it alters earth pressure distribution around the lining. When anisotropy is applied selectively to different ground layers, tunnel deformation varies but always falls between the fully anisotropic and isotropic cases. Additionally, 3D effects play a crucial role, as high-permeability layers can affect tunnel sections embedded in low-permeability ground. These findings highlight the importance of considering permeability anisotropy in long-term tunnel assessments, as neglecting it may lead to inaccurate deformation predictions.

The three-dimensional finite element modelling results provide a comprehensive understanding of the long-term behaviour of the CERN TT10 tunnel, considering the effect of tunnel deteriorations, swelling marl, ground layering, and permeability anisotropy. The tunnel's inclined alignment and highly variable ground conditions lead to differential displacement, tunnel alignment issues, cracking, and other ageing defects at different sections. Among these factors, swelling marl is identified as the primary driver of long-term tunnel deformation, with hydraulic and mechanical deterioration playing secondary roles. In this study, tunnel deterioration was modelled under simplified conditions with predefined timeframes. However, in reality, its progression is influenced by factors such as groundwater conditions, external disturbances, and maintenance interventions. Accurately predicting long-term tunnel behaviour requires both temporally continuous and spatially continuous field monitoring and adaptive modelling to refine predictions as new data becomes available.

Despite its contributions, this study has some limitations, including simplified models and assumptions such as Mohr-Column model, uniform lining permeability and linear deterioration trends, which may not fully capture the realistic performance and localised effects. For example, in this study, the Mohr-Coulomb model was used to simulate rock behaviour due to its simplicity, computational efficiency and stability, and common use in geotechnical applications. In addition, the stress level of the rock around the tunnel still largely remains within the elastic domain, which may be generally considered using Mohr-Coulomb model. However, MC model has limitations, particularly in capturing non-linear post-peak softening, dilation evolution, and confinement-dependent strength, which may be important for more detailed time-dependent ground modelling. While this model provides a practical approximation for the overall deformation analysis of the tunnel, more advanced models could offer better insight into these complex behaviours but would require additional calibration and data, which is beyond the scope of this study. Regarding deterioration models, in practice, drainage degradation and lining leakage/clogging are often localised (e.g., partial blockage of drains, preferential clogging at specific sections, or localised cracking/spalling), which can lead to spatially non-uniform pore-pressure build-up around and along the tunnel. Such heterogeneity may produce more localised deformation features (e.g., asymmetric ovalisation/distortion and larger local displacement gradients) than those predicted by the present homogenised model, and may shift the deformation pattern locally even if the overall mechanism remains the same. In addition, given the absence of time-resolved hydraulic conductivity measurements, the permeability reduction is treated to be linearly evolving as a bounded scenario between an initial 'drained' state and an end-state 'clogged' condition. While this provides a transparent first-order approximation, alternative non-linear deterioration trajectories could alter the timing of pore-pressure build-up and deformation development. However, the modelling and investigation of

these effects quantitatively would require additional spatially varied hydraulic and condition data in detail (e.g., section-by-section drainage performance, leakage mapping, or distributed measurements), which is currently unavailable in CERN and therefore requires future research work. Additionally, a lack of more comprehensive field data (e.g., spatially continuous measurements) limits the precision of model validation. Future research should explore more localised deterioration effects, integrate field-test-based deterioration modelling, and consider additional degradation mechanisms such as sulphate attack, carbonation, freeze-thaw cycles, groundwater erosion, and chloride-induced reinforcement corrosion. In addition, no formal sensitivity analysis (with quantitative sensitivity indices) is performed with regard to the parametric study; instead, parameter influence is inferred from bounded scenario comparisons in Section 5. Future work will implement formal sensitivity analysis once parameter ranges can be constrained more robustly by additional monitoring and site characterisation data. Addressing these areas can further advance our understanding of the long-term performance of tunnels in a more realistic and comprehensive manner.

Funding

This work was supported by Irish Research Council and the European Union's Horizon 2020 research and innovation programme under the-Marie Skłodowska-Curie grant agreement no. 713279 (Grant number: CLNE/2019/199).

Data availability

The datasets generated during and/or analysed during the current study are available from the corresponding author on reasonable request.

CRediT authorship contribution statement

Zhipeng Xiao: Writing – review & editing, Writing – original draft, Methodology, Investigation, Funding acquisition, Formal analysis, Data curation, Conceptualization. **Chao Wang:** Writing – review & editing, Writing – original draft, Methodology, Investigation, Formal analysis, Data curation. **Chuanyang Peng:** Writing – review & editing, Investigation, Formal analysis. **John Andrew Osborne:** Writing – review & editing, Supervision, Resources. **Zili Li:** Writing – review & editing, Supervision, Conceptualization.

Declaration of interests

The authors declare that they have no known competing financial interests or personal relationships that could have appeared to influence the work reported in this paper.

Acknowledgements

This research work was funded by Irish Research Council and the European Union's Horizon 2020 research and innovation programme under the Marie Skłodowska-Curie grant agreement no. 713279. The financial support is gratefully acknowledged. The authors also would like to thank Prof. Kenichi Soga (University of California, Berkeley) and Dr. Vanessa Di Murro (CERN) for their valuable advice and assistance in this CERN tunnel project.

References

Bonini, M., Debernardi, D., Barla, M., & Barla, G. (2009). The mechanical behaviour of clay shales and implications on the design of tunnels. *Rock Mechanics and Rock Engineering, 42*, 361–388. https://doi.org/10.1007/s00603-007-0147-6

CERN. (1972). *The 300 gev programme*. Geneva: CERN.

Di Murro, V., Pelecanos, L., Soga, K., Kechavarzi, C., Morton, R., & Scibile, L. (2016). Distributed fibre optic long-term monitoring of concrete-lined tunnel section TT10 at CERN. In *Proceedings of the International Conference on Smart Infrastructure and Construction* (pp. 27–32). ICE Publishing. https://doi.org/10.1680/tfitsi.61279.027.

Di Murro, V. (2019). *Long-Term performance of a concrete-lined tunnel at CERN*. University of Cambridge, UK: Department of Engineering.

Do, D.-P., Tran, N.-T., Mai, V.-T., Hoxha, D., & Vu, M.-N. (2020). Time-dependent reliability analysis of deep tunnel in the viscoelastic burger rock with sequential installation of liners. *Rock Mechanics and Rock Engineering, 53*, 1259–1285. https://doi.org/10.1007/s00603-019-01975-6

Fern, E. J., Di Murro, V., Soga, K., Li, Z., Scibile, L., & Osborne, J. A. (2018). Geotechnical characterisation of a weak sedimentary rock mass at CERN. *Geneva Tunnelling and Underground Space Technology, 77*, 249–260. https://doi.org/10.1016/j.tust.2018.04.003

GADZ, 2016a. Reconnaissances géotechnique point 1 – No 7222/2. Technical report, Géotechnique Appliquée Dériaz SA (in French).

GADZ, 2016b Reconnaissances géotechnique point 5 – No 7223/2. Technical report, Géotechnique Appliquée Dériaz SA (in French).

Idris, J., Al-Heib, M., & Verdel, T. (2009). Numerical modelling of masonry joints degradation in built tunnels. *Tunnelling and Underground Space Technology, 24*, 617–626. https://doi.org/10.1016/j.tust.2009.05.002

Jang, Y.-S., Kim, B., & Lee, J.-W. (2015). Evaluation of discharge capacity of geosynthetic drains for potential use in tunnels. *Geotextiles and Geomembranes, 43*, 228–239. https://doi.org/10.1016/j.geotexmem.2015.03.00

Jung, H. S., Han, Y. S., Chung, S. R., Chun, B. S., & Lee, Y. J. (2013). Evaluation of advanced drainage treatment for old tunnel drainage system in Korea. *Tunnelling and Underground Space Technology, 38*, 476–486. https://doi.org/10.1016/j.tust.2013.08.004

Kim, K. H., Park, N. H., Kim, H. J., & Shin, J. H. (2020). Modelling of hydraulic deterioration of geotextile filter in tunnel drainage system. *Geotextiles and Geomembranes, 48*, 210–219. https://doi.org/10.1016/j.geotexmem.2019.11.008

Kovári, K., & Staus, J. (1996). Basic considerations on tunnelling in squeezing ground. *Rock Mechanics and Rock Engineering, 29*, 203–210. https://doi.org/10.1007/BF01042533

Laver, R.G., Li, Z., and Soga, K. 2017. Method to evaluate the long-term surface movements by tunneling in London clay. Journal Geotechnical Geoenvironmental Engineering, 143: 06016023. doi:10.1061/(ASCE)GT.1943-5606.0001611.

Li, Z., Soga, K., & Wright, P. (2015). Long-term performance of cast-iron tunnel cross passage in London Clay. *Tunnelling and Underground Space Technology, 50*, 152–170. https://doi.org/10.1016/j.tust.2015.07.005

Li, Z., Soga, K., & Wright, P. (2016). Three-dimensional finite element analysis of the behaviour of cross passage between cast-iron tunnels. *Candian Geotechnical Journal, 53*, 930–945. https://doi.org/10.1139/cgj-2015-0273

Li, P., Liu, H., Zhao, Y., & Li, Z. (2018). A bottom-to-up drainage and water pressure reduction system for railway tunnels. *Tunnelling and Underground Space Technology, 81*, 296–305. https://doi.org/10.1016/j.tust.2018.07.027

Li, W., Afshani, A., Akagi, H., & Oka, S. (2020). Influence of lining permeability and temperature on long-term behavior of segmented tunnel. *Soils and Foundations, 60*, 425–438. https://doi.org/10.1016/j.sandf.2020.03.005

Liu, G., Chen, Y., Du, X., & Azzam, R. (2021). A fractional viscoplastic model to predict the time-dependent displacement of deeply buried tunnels in swelling rock. *Computers and Geotechnics, 129*, Article 103901. https://doi.org/10.1016/j.compgeo.2020.103901

Murillo, C. A., Shin, J. H., Kim, K. H., & Colmenares, J. E. (2014). Performance tests of geotextile permeability for tunnel drainage systems. *KSCE Journal of Civil Engineering, 18*, 827–830. https://doi.org/10.1007/s12205-014-0753-2

Nie, X., & Zhang, Q. (1994). A system of monitoring and dimensioning tunnel support. *Rock Mechanics and Rock Engineering, 27*, 23–36. https://doi.org/10.1007/BF01025954

Reddi, L. N., Ming, X., Hajra, M. G., & Lee, I. M. (2000). Permeability reduction of soil filters due to physical clogging. *Journal of Geotechnical and Geoenvironmental, 126*, 236–246. https://doi.org/10.1061/(ASCE)1090-0241(2000)126:3(236)

Sandrone, F., & Labiouse, V. (2010). Analysis of the evolution of road tunnels equilibrium conditions with a convergence–confinement approach. *Rock Mechanics and Rock Engineering, 43*, 201–218. https://doi.org/10.1007/s00603-009-0056-y

Shin, J. H., Potts, D. M., & Zdravkovic, L. (2005). The effect of pore-water pressure on NATM tunnel linings in decomposed granite soil. *Candian Geotechnical Journal, 42*, 1585–1599. https://doi.org/10.1139/t05-072

Shin, J. H., Kim, S. H., Chae, S. E., & Kwon, O. Y. (2010). Hydraulic deterioration and significance of tunnel drainage systems. In *Proceedings World Tunnel Congress 2010, ITA-AITES* (pp. 1–8).

Shin, J. H., Kim, S. H., & Shin, Y. S. (2012). Long-term mechanical and hydraulic interaction and leakage evaluation of segmented tunnels. *Soils Found, 52*, 38–48. https://doi.org/10.1016/j.sandf.2012.01.011

Shin, J.-H., Lee, I.-K., & Joo, E.-J. (2014). Behavior of double lining due to long-term hydraulic deterioration of drainage system. *Structural Engineering and Mechanics, 52*, 1257–1271. https://doi.org/10.12989/sem.2014.52.6.1257

Shin, J. H. (2008). Numerical modeling of coupled structural and hydraulic interactions in tunnel linings. *Structural Engineering and Mechanics, 29*, 1–16. https://doi.org/10.12989/sem.2008.29.1.001

Showkati, A., Salari-rad, H., & Hazrati Aghchai, M. (2021). Predicting long-term stability of tunnels considering rock mass weathering and deterioration of primary support. *Tunnelling and Underground Space Technology, 107*, Article 103670. https://doi.org/10.1016/j.tust.2020.103670

Tornborg, J., Karlsson, M., Kullingsjö, A., & Karstunen, M. (2021). Modelling the construction and long-term response of Göta Tunnel. *Computers and Geotechnics, 134*, Article 104027. https://doi.org/10.1016/j.compgeo.2021.104027

Usman, M., & Galler, R. (2013). Long-term deterioration of lining in tunnels. *International Journal of Rock Mechanics and Mining Science, 64*, 84–89. https://doi.org/10.1016/j.ijrmms.2013.08.028

Wang, R., Li, L., 2018. Burgers creep model used for describing and predicting the creep behaviour of a rock under uniaxial and triaxial compression test conditions.

Wang, Z., Wong, R. C. K., Li, S., & Qiao, L. (2012). Finite element analysis of long-term surface settlement above a shallow tunnel in soft ground. *Tunnelling and Underground Space Technology, 30*, 85–92. https://doi.org/10.1016/j.tust.2012.02.010

Wang, R., Li, L., & Simon, R. (2019). A model for describing and predicting the creep strain of rocks from the primary to the tertiary stage. *International Journal of Rock Mechanics and Mining Sciences, 123*, Article 104087. https://doi.org/10.1016/j.ijrmms.2019.104087

Wang, Y., Liu, Y., Wang, Z.-F., Zhang, X., Hui, Y., & Li, J. (2023). Investigation on progressive failure process of tunnel lining induced by creep effect of surrounding rock: A case study. *Engineering Failure Analysis, 144*, Article 106946. https://doi.org/10.1016/j.engfailanal.2022.106946

Wang, C., Xiao, Z., Friedman, M., & Li, Z. (2024). Modelling the impact of deterioration on the long-term performance of Dublin Tunnel. *Canadian Geotechnical Journal, 62*, 1–20. https://doi.org/10.1139/cgj-2024-0296

Wang, C., Xiao, Z., Frieman, M., & Li, Z. (2025). Modelling the impact of deterioration on the long-term performance of Dublin Tunnel. *Canadian Geotechnical Journal, 62*. https://doi.org/10.1139/cgj-2024-0296

Wongsaroj, J., Soga, K., & Mair, R. (2007). Modelling of long-term ground response to tunnelling under St James's Park, London. *Geotechnique, 57*, 75–90. https://doi.org/10.1680/geot.2007.57.1.75

Wongsaroj, J., Soga, K., & Mair, R. J. (2013). Tunnelling-induced consolidation settlements in London Clay. *Geotechnique, 63*, 1103–1115. https://doi.org/10.1680/geot.12.P.126

Wu, H. N., Huang, R. Q., Sun, W. J., Shen, S. L., Xu, Y. S., Liu, Y. B., & Du, S. J. (2014). Leaking behavior of shield tunnels under the Huangpu River of Shanghai with induced hazards. *Nature Hazards, 70*, 1115–1132. https://doi.org/10.1007/s11069-013-0863-z

Wu, H. N., Shen, S. L., Chen, R. P., & Zhou, A. (2020). Three-dimensional numerical modelling on localised leakage in segmental lining of shield tunnels. *Computers and Geotechnics, 122*. Three-dimensional numerical modelling on localised leakage in segmental lining of shield tunnels.

Xiao, Z., Di Murro, V., Osborne, J., Zhu, H., & Li, Z. (2024). Distributed fibre optic sensing and novel data processing method for tunnel circumferential deformation – A case study of an ageing tunnel at CERN. *Tunnelling and Underground Space Technology, 153*, Article 106014. https://doi.org/10.1016/j.tust.2024.106014

Yang, W., Zhang, Q., Li, S., & Wang, S. (2014). Time-dependent behavior of diabase and a nonlinear creep model. *Rock Mechanics and Rock Engineering, 47*, 1211–1224. https://doi.org/10.1007/s00603-013-0478-4

Yokozeki, K., Watanabe, K., Sakata, N., & Otsuki, N. (2004). Modeling of leaching from cementitious materials used in underground environment. *Applied Clay Science, 26*, 293–308. https://doi.org/10.1016/j.clay.2003.12.027

Yoo, C. (2016). Hydraulic deterioration of geosynthetic filter drainage system in tunnels – its impact on structural performance of tunnel linings. *Geosynthetics International, 23*, 463–480. https://doi.org/10.1680/jgein.16.00010

Yoo, C. (2017). Effect of water leakage in tunnel lining on structural performance of lining in subsea tunnels. *Marine Georesources and Geotechnology, 35*, 305–317. https://doi.org/10.1080/1064119X.2016.1162235

Zhang, D. M., Ma, L. X., Zhang, J., Hicher, P. Y., & Juang, C. H. (2015). Ground and tunnel responses induced by partial leakage in saturated clay with anisotropic permeability. *Engineering Geology, 189*, 104–115. https://doi.org/10.1016/j.enggeo.2015.02.005

Zhang, D. M., Huang, Z. K., Yin, Z. Y., Ran, L. Z., & Huang, H. W. (2017). Predicting the grouting effect on leakage-induced tunnels and ground response in saturated soils. *Tunnelling and Underground Space Technology, 65*, 76–90. https://doi.org/10.1016/j.tust.2017.02.00

Zhang, X., Wei, C., & Zhang, H. (2021). Analysis of surrounding rock creep effect on the long-term stability of tunnel secondary lining. *Shock and Vibration, 2021*, Article 4614265. https://doi.org/10.1155/2021/4614265

Zhang, S., Xu, Q., Yoo, C., Min, B., Liu, C., Guan, X., & Li, P. (2022). Lining cracking mechanism of old highway tunnels caused by drainage system deterioration: A case study of Liwaiao Tunnel, Ningbo, China. *Engineering Failure Analysis, 137*, Article 106270. https://doi.org/10.1016/j.engfailanal.2022.106270